Journal of Materials Research and Technology 41 (2026) 5474–5488

Contents lists available at ScienceDirect

Journal of Materials Research and Technology

journal homepage: www.elsevier.com/locate/jmrt

Corrosion resistance investigation of Cronidur30 high-nitrogen martensitic stainless steel by quasi-in-situ SKPFM and DFT calculation

Xiaoqian Fu [a], Yucheng Ji [a,*], Chao Liu [a], Wentao Qin [a], Cunyu Wang [b], Wenquan Cao [b,**], Poulumi Dey [c], Xuequn Cheng [a], Jianxiong Liang [b], Chaofang Dong [a,***]

[a] Beijing Advanced Innovation Center for Materials Genome Engineering, National Materials Corrosion and Protection Data Center, Institute for Advanced Materials and Technology, University of Science and Technology Beijing, Beijing, 100083, China
[b] Special Steel Department, Central Iron and Steel Research Institute (CISRI), Beijing, 100081, China
[c] Department of Materials Science and Engineering, Faculty of Mechanical Engineering, Delft University of Technology, 2628CD, Delft, the Netherlands

ARTICLE INFO

Keywords:
High-nitrogen martensitic stainless steel
Precipitates
Passive film
Corrosion

ABSTRACT

Nitrogen alloying improves the mechanical performance of martensitic stainless steel, while tempering is required to mitigate brittleness and enhance processability. However, tempering-induced microstructural changes markedly influence the semiconducting properties of the passive film, thereby affecting corrosion resistance. This work examines the passive film of high-nitrogen martensitic stainless steel (HNMSS) tempered at different temperatures. Tempering at 200 °C yields the highest pitting potential (461.28 mV), attributed to the transformation of CrN to Cr_2O_3, which enhances film protection. At higher temperatures, abundant Cr-rich nitride/precipitate (M_2N) depletes N and Cr in the matrix. The increase of precipitate/matrix interfaces and defect density in the passivation film impairs pitting corrosion resistance. First-principles calculations and quasi-in-situ scanning Kelvin probe force microscopy reveal that M_2N precipitates exhibit a higher Volta potential and the highest work function than those of the matrix, acting as cathodes to accelerate localized matrix dissolution, which reduces nitrogen incorporation into the passive film. These findings clarify the relationship of tempering, microstructure, and corrosion in the HNMSS.

1. Introduction

As a third generation of bearing materials, high-nitrogen martensitic stainless steel (HNMSS) is widely used in marine and aerospace applications owing to its high strength, good corrosion resistance, and fatigue performance [1–3]. Interstitial nitrogen plays a critical role in improving both strength and toughness of steel via solid solution strengthening [4,5]. As a strong austenite-stabilizing element that substitutes C in stainless steel, N also influences the microstructure, including the volume fraction of retained austenite (RA) [6], grain size [7], martensite morphology [8], and the types of precipitates [9,10].

The presence of N can promote the enrichment of Cr in the passive film, reduce point defect density, and increase the thickness of the passive film [11,12]. Therefore, N can decrease the sensitivity to metastable pitting and enhance the repassivation ability and corrosion resistance, particularly in Cl^- solutions [13–15]. Chen et al. [16] demonstrated that N can reduce the acidity of the surface passive film and enhance the electronic properties of repelling Cl^- ions. Moreover, according to the well-known pitting resistance equivalent number (PREN) [17], N has a higher proportionality coefficient than Cr and Mo, which further explains that N is an effective alloying element for enhancing the pitting resistance of stainless steels.

However, Cronidur30 martensitic stainless steel with high C and N content requires heat treatment to achieve reliable mechanical properties, inevitably leading to a complex microstructure [18,19]. This includes a martensitic matrix with various crystallographic orientations, retained austenite, and both nano- and microscale carbide and nitride precipitates [20–22]. Such heterogeneous structure makes it challenging to elucidate the resulting variations in the chemical composition of the passive film. Previous studies have shown that the passive film on stainless steel generally exhibits a homogeneous bilayer structure [23]. The outer layer is composed of iron oxides and hydroxides formed

* Corresponding author.
** Corresponding author.
*** Corresponding author.
E-mail addresses: jiyucheng@ustb.edu.cn (Y. Ji), caowenquan@nercast.com (W. Cao), cfdong@ustb.edu.cn (C. Dong).

https://doi.org/10.1016/j.jmrt.2026.02.120
Received 10 January 2026; Received in revised form 12 February 2026; Accepted 14 February 2026
Available online 16 February 2026

through the dissolution and redeposition of metal cations, whereas the inner layer mainly consists of Cr-rich oxides. However, on surfaces containing significant amounts of carbides and nitrides, the oxidation behavior differs distinctly between the precipitates and the metallic matrix owing to their different thermodynamic stabilities, particularly in the case of the abundant Cr_2N precipitates in N-alloyed stainless steels [24,25]. In addition, the precipitation of Cr_2N consumes Cr from the surrounding matrix, thereby reducing the protective capability of the passive film. Therefore, understanding how the oxidation behavior of such heterogeneous surfaces affects corrosion performance is essential.

Currently, scanning Kelvin probe force microscopy (SKPFM) is a widely used technique for characterizing surface morphology and determining the Volta potential distributions of materials. By detecting surface Volta potential through a Kelvin probe, the susceptibility of a material to corrosion can be assessed. This method has been widely employed to study the corrosion resistance of passive film formed on steel surfaces, including duplex, austenitic, and martensitic stainless steels. For instance, Man et al. [23] studied the nanostructure of passive film formed on AM355 martensitic stainless steel at different formation potentials by SKPFM. Meanwhile, this technology is of great importance for studying the localized corrosion process of materials with complex nano-scale and micron-scale surface features [26]. For instance, Li et al. [27] found that the pits in austenitic stainless steel welded joints initiate and propagate along the H-rich α/γ interface by conducting an SKPFM test. Additionally, Hai et al. [28] found that the Volta potentials of RA/inverted austenite and grain boundaries were higher than those of the matrix in NiCrMoV/Nb high-strength steels. However, due to the lack of in-situ techniques capable of directly observing the growth of passive films on precipitates and the surrounding matrix, it remains difficult to capture the initiation and propagation of localized corrosion associated with these precipitates.

Therefore, first-principles calculations based on density functional theory (DFT) at the atomic scale are necessary to predict the corrosion tendencies [29–31]. For example, Ji et al. [32] performed high-throughput DFT calculations to evaluate the work functions of secondary phases in Al alloys and identified Cu-doped Al–Sc precipitates as highly effective in trapping H atoms, thereby improving corrosion resistance. Similarly, Xue et al. [33] demonstrated through DFT calculations combined with AFM measurements that the Al_7Cu_2Fe phase exhibited a higher work function and produced a larger potential difference with the surrounding matrix, which can drive earlier corrosion initiation in the matrix.

This study aims to investigate the key factors affecting the corrosion resistance of HNMSS. To establish an intrinsic link between atomistic electrochemical mechanisms and macroscopic corrosion behavior, DFT calculations are conducted to determine the work function and Fermi level of carbide and nitride precipitates relative to the matrix. Combining these calculation results with SKPFM measurements, the Volta potential differences (VPDs) between precipitates and the surrounding matrix were revealed. Quasi-in-situ observations were subsequently carried out to validate the consistency between the SKPFM-measured Volta potentials and the DFT predictions. Finally, electrochemical tests and X-ray photoelectron spectroscopy (XPS) are used to characterize the passive film of the steel after various heat treatments, and to evaluate the influence of nano/sub-micron nitride and carbide precipitates on its corrosion behavior.

2. Materials and methods

2.1. Material and sample preparation

Cronidur30 HNMSS was prepared via the pressure electroslag remelting and refining routes, and its chemical composition is listed in Table 1. The hot-forged Cronidur30 steel was first homogenized at 870 °C for 4 h, then cooled to 730 °C and heated for 3 h until the furnace cooled to room temperature. Subsequently, these samples were treated to austenitize at 1050 °C for 30 min followed by water quenching, and soaked in liquid nitrogen (−196 °C) via cryogenic treatment for 2 h. Subsequently, double tempering was performed at 200 °C, 350 °C, 470 °C, 500 °C, and 550 °C for 2 h, respectively, immediately cooling in air. The heat treatment process is depicted in Fig. 1.

2.2. Electrochemical measurement

Electrochemical testing solution for HNMSS contained 3.5 wt% NaCl, and its sample size was 10 mm × 10 mm × 3 mm, embedded in epoxy resin. Then, the samples were mechanically polished using 1 μm diamond powder and cleaned with alcohol. A VersaStudio 3F electrochemical workstation equipped with a traditional three-electrode system was used for the process. Prior to all the tests, each sample was cathodically polarized at −1 V_{SCE} for 300 s to reduce the air-formed passive film. The samples were first immersed for 40 min in the solution to obtain the open circuit potential (OCP) and make the system relatively stable. Subsequently, the EIS test was monitored at OCP over a frequency range from 100 kHz to 10 mHz, with a signal amplitude perturbation voltage of 10 mV. Potentiodynamic polarization measurements were performed with a scanning rate of 0.333 mV/s from −500 mV (vs. OCP) to an anodic current density of 1 mA/cm^2. To further clarify the electrochemical reaction processes occurring in the samples subjected to different tempering treatments as the applied potential varies, cyclic voltammetry (CV) measurements were conducted at a scan rate of 50 mV/s, with all tests started at an initial potential of −1.2 V_{SCE}. The HNMSS samples were subjected to potentiostatic polarization at −100 mV_{SCE} for 1 h to form a stable passive film in NaCl solutions and investigate the influence of the tempering temperature on the properties

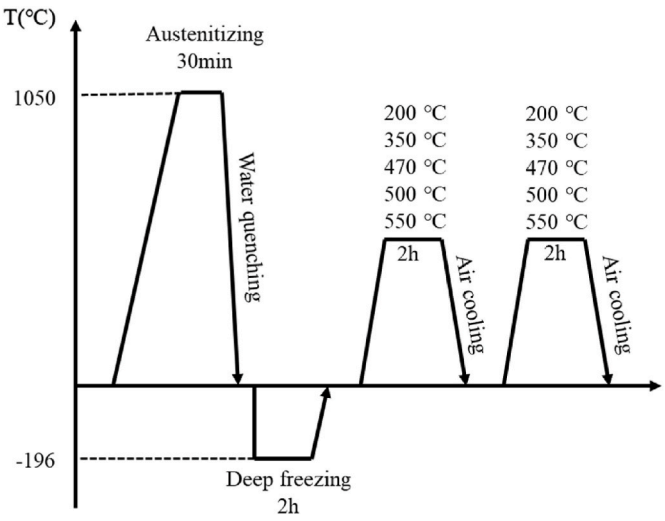

Fig. 1. Schematic of the heat treatment process of HNMSS.

Table 1
Chemical composition of HNMSS (wt.%).

C	N	Si	Mn	P	S	Cr	Ni	Cu	Mo	V	Fe
0.3	0.38	0.066	0.44	0.0078	0.0011	15.42	0.2	0.032	0.95	0.05	Bal.

of the passive film. Meanwhile, Mott–Schottky experiments were performed at 25 mV/s from −1 V_{SCE} to 1 V_{SCE} with an amplitude of 10 mV at 1 kHz.

2.3. Microstructure analysis and corrosion morphology observation

The volume fraction of RA with tempered samples was determined by X-ray Diffraction (XRD) technique (using Cu Kα radiation at a scanning speed of 2°/min in the 2θ range from 30° to 110°. The calculations were based on the integrated intensities of $(110)_\alpha$ martensite peaks, as well as $(111)_\gamma$ austenite diffraction peaks. The volume fraction of RA was determined by Eq. (1):

$$V_A = \frac{1.4I_\gamma}{I_\alpha + 1.4I_\gamma} \quad (1)$$

where I_γ and I_α are the integrated intensities of $(111)_\gamma$ and $(110)_\alpha$, respectively.

After the potentiodynamic polarization tests, the corrosion morphologies were examined using an FEI Quanta 250 scanning electron microscope (SEM) equipped with an energy dispersive spectroscope (EDS) at an accelerating voltage of 20 kV and a working distance of 15 mm to obtain SEM back-scattered electron (BSE) and secondary electron (SE) images. EBSD analysis was performed using a field-emission gun Zeiss Gemini 500 SEM equipped with an Oxford Symmetry EBSD detector after being polished using a 50 nm SO-T402 colloidal silica suspension for at least 40 min. The EBSD pattern was recorded at a step size of 0.02 μm and subsequently analyzed using the AZtecCrystal software. The detailed crystal structure of the microstructures was analyzed using an FEI Tecnai G^2 F20 transmission electron microscope (TEM), while the Φ3 mm samples were electropolished with a solution of 5 vol% perchloric acid and 95 vol% acetic acid at 30 V.

2.4. XPS surface analysis

The tempered samples polarized at −0.1 V_{SCE} for 1 h were used to characterize the variation in the passive films. XPS analysis was conducted using the Thermo ESCALAB 250 XI spectrometer with a monochromatic Al Kα radiation source. All the XPS peaks were fitted with the Xpspeak version 4.1 software, which contained Shirley background subtraction and Gaussian–Lorentzian product function. Charge calibration was performed before fitting, and the peak at the lowest binding energy end of C1s spectrum was calibrated to 284.8 eV.

2.5. SKPFM test

SKPFM specimens were first polished using a 0.5 μm diamond paste, followed by light etching with colloidal silica suspension for 5 min. The experiment was conducted using a Bruker MultiMode 8 atomic force microscope system (Germany). The probe model used was APFQNE-AL, with a stiffness of 0.8 N/m and a resonance frequency of 300 kHz. The probe was operated in tapping mode with a scan rate of 0.498 Hz and a pixel resolution of 512 × 512. All SKPFM tests were performed in an air atmosphere at 25 °C with an approximate relative humidity of 45%.

2.6. DFT calculations

The Vienna Ab-initio Simulation Package (VASP 6.4) was used to perform DFT calculations for austenite, martensite, M_2N, and $M_{23}C_6$, whose orientations were extracted from the experimental EBSD. The austenite primitive structure was face-centered cubic (FCC) Fe (Fm $\bar{3}$ m), with one C distributed at the octahedral interstitial site, while the martensite primitive structure was body-centered cubic (BCC) Fe (Im$\bar{3}$ m) with C atoms at the octahedral interstitial sites. The austenite primitive structure contained four Fe atoms and one C atom, and the martensite primitive structure contained 128 Fe atoms and 4 C atoms.

The primitive structures of M_2N and $M_{23}C_6$ were P $\bar{3}$ 1 m and Fm$\bar{3}$ m. Based on the EBSD-detected orientations, the surface work function calculation used generalized gradient approximation (GGA) and the Perdew–Burke–Ernzerhof exchange-correlation functional (PBE). The vacuum thickness of surface models was 15 Å, and the electron and force convergence accuracies were 10^{-5} eV and 0.01 eV/Å. The cut-off energy was 450 eV, and the *k*-points spatial length was lower than 0.25/Å. All initial calculation models and equivalent sites are shown in Fig. 2. The work function was calculated using Eq. (2)

$$\psi = \phi - E_{fermi} \quad (2)$$

where ϕ indicates the average potential in the vacuum gap. E_{fermi} indicates the Fermi level.

3. Results and discussion

3.1. Effect of tempering treatment on microstructures of HNMSS

The XRD patterns of HNMSS after tempering treatments are summarized in Fig. 3a, it can be found that the matrix is primarily composed of martensite (I4/mmm) and austenite (Im$\bar{3}$ m). The martensite (110) peak exhibits the strongest intensity, and with the increase in tempering temperature, the intensity of the austenite peak (2θ = 43.53°) significantly decreases. As shown in Fig. 3b, the content of RA in the samples is calculated using Eq. (1). The volume fractions of RA at tempering temperatures of 200 °C, 350 °C, 470 °C, 500 °C, and 550 °C are 28.5%, 25.6%, 20.5% 12.3%, and 0%, respectively.

In the temperature range of 200 °C to 470 °C, the RA content changes slowly. However, when the temperature rises beyond 470 °C to 550 °C, the RA content in the samples sharply decreases. At 550 °C, the characteristic peaks of austenite disappear. M_2N nitrides peaks appear in all samples identified by using space group P $\bar{3}$ 1 m for Cr_2N nitrides (PDF Card number 19-0030). It is reported that $M_{23}C_6$ carbides are nearly fully dissolved at the solution treatment temperature of 1050 °C, which results in the absence of discernible diffraction peaks in the XRD result [6].

3.2. Surface morphology and volta potential variations between the phases

It is reported that the main precipitates in HNMSS include nitrides and carbides within the temperature range of 200°C-550 °C, specifically M_2N (M = Fe, Cr) and $M_{23}C_6$ [6,34]. Due to the relatively high N content in Cronidur30 HNMSS, a significant fraction of RA remains after tempering treatment, and this fraction decreases as the tempering temperature increases [35]. To evaluate the influence of the five samples with distinct and complex microstructures on their local corrosion behavior, SKPFM measurements are conducted in air. The corresponding Volta potential distribution maps are shown in Fig. 4a–e. It can be found that the precipitates exhibit irregular morphologies, primarily appearing as spherical or rod-like structures, and their Volta potentials are significantly higher than those of the surrounding matrix.

The statistical distribution of VPDs between the precipitates and the matrix within the 20 μm × 20 μm scanned area is presented in Fig. 4f, showing that this potential difference increases as the tempering temperature rises. Moreover, the 200 °C sample shows the VPD of approximately 30 mV, which increases to roughly 50 mV for the 550 °C sample. Recent studies have demonstrated that the size, type, and volume fraction of precipitates in high-nitrogen steels significantly affect their corrosion resistance, and the interfaces of precipitate and surrounding matrix are vulnerable to attack by aggressive ions, which promotes localized corrosion [36].

In addition, the influence of precipitate size on the measured Volta potential was found to be significant across the five samples. Fig. 5a–e presents the distribution of the potential difference between precipitates

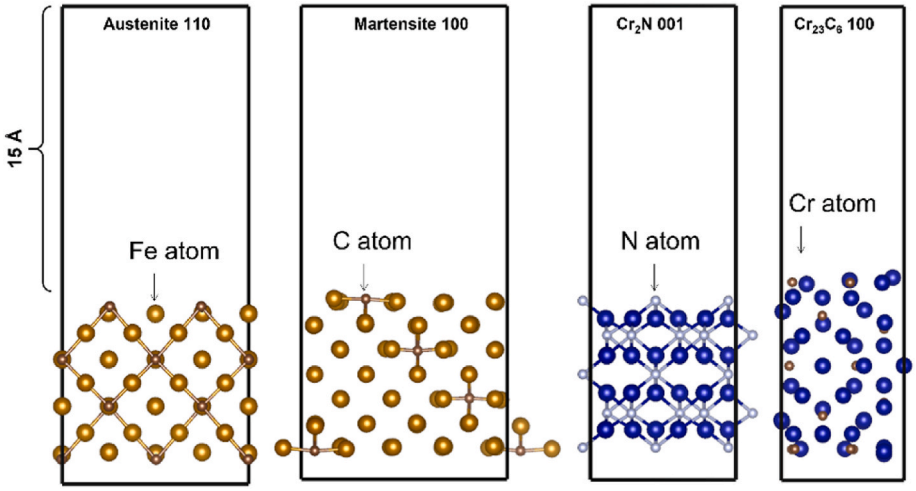

Fig. 2. Surface models used in DFT calculation with 15 Å vacuum.

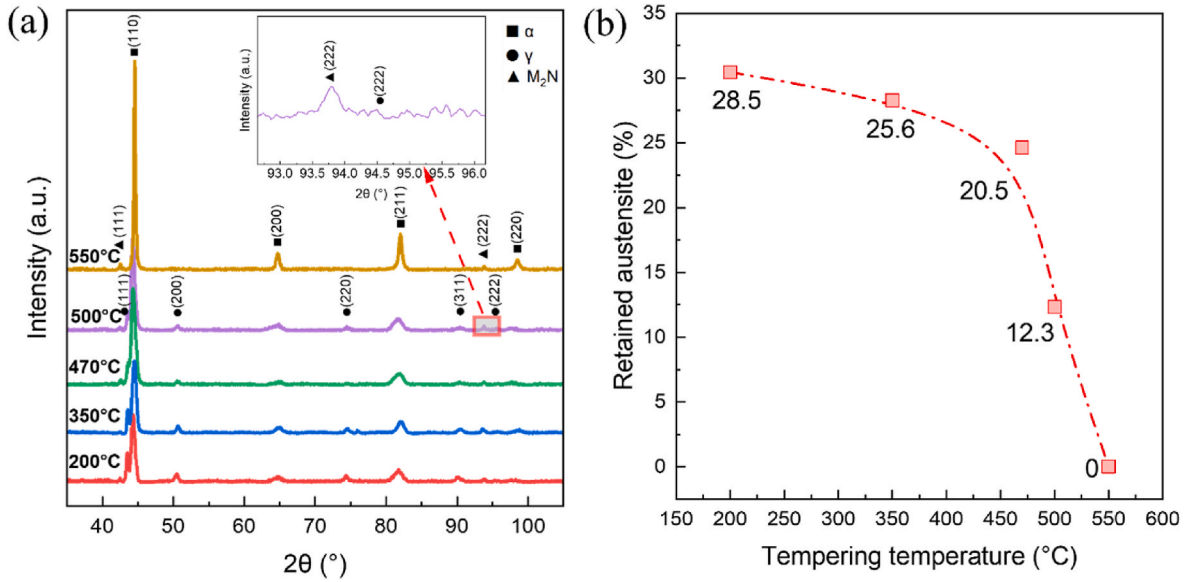

Fig. 3. The matrix analysis of HNMSS with different heat treatments: (a) XRD spectra; (b) the variation of RA content with tempering temperatures by XRD.

and the matrix as a function of precipitate size, and a consistent trend is observed that smaller precipitates exhibit lower VPDs. Notably, the proportion of nanoscale precipitates increases in the 550 °C sample, with the potential difference between 1 μm precipitates and the matrix reaching approximately 70 mV. According to the fitting results shown in Fig. 5f, the 550 °C sample exhibits the steepest quantitative dependence (slope), indicating that the influence of precipitate size on the potential difference is more sensitive in the high-temperature samples compared with the low-temperature tempered samples.

3.3. Corrosion resistance evaluation of HNMSS at different tempering temperatures

The potentiodynamic polarization curves of HNMSS tempered at different temperatures in 3.5 wt.% NaCl solutions are summarized in Fig. 6a and b. Evidently, all samples exhibit a distinct passive region. Despite altering the microstructure, the tempering treatment does not impair the ability of the steel to form a protective passive film, which is crucial for its corrosion resistance in Cl-containing environments.

The corrosion potential (E_{corr}), pitting potential (E_{pit}), and passive current density (i_p) acquired from the potentiodynamic polarization curves are presented in Table 2. The 200 °C tempered sample exhibits the highest E_{pit} (461.28 mV), and the E_{pit} sharply decreases while i_p increases with the tempering temperature. When the potential exceeds E_{pit}, the current density rises rapidly, indicating breakdown of the passive film and the initiation of pitting corrosion. Additionally, i_p increases from 0.836 to 1.333 μA/cm^2 as the tempering temperature rises, thus indicating a higher corrosion rate for the sample tempered at a higher temperature. The different tempering treatments do not change the cathodic kinetics of HNMSS, where oxygen reduction occurs as the cathodic reaction in neutral NaCl solutions. The differences in the electrochemical behavior of the samples are primarily influenced by the properties of the passive film, including its composition, thickness, and compactness [23,37].

More importantly, the primary factor determining the performance of the passive film is the microstructure of the HNMSS. At a lower temperature (200 °C), the solid solution of N in the matrix and the presence of a large amount of RA can significantly enhance the pitting corrosion resistance of stainless steel [38]. It has already been shown that the Cr-depleted regions in the HNMSS adjacent to the grain boundary Cr-rich carbides/nitrides precipitate act as a discontinuity, and that the chemical changes in the interface region influence the

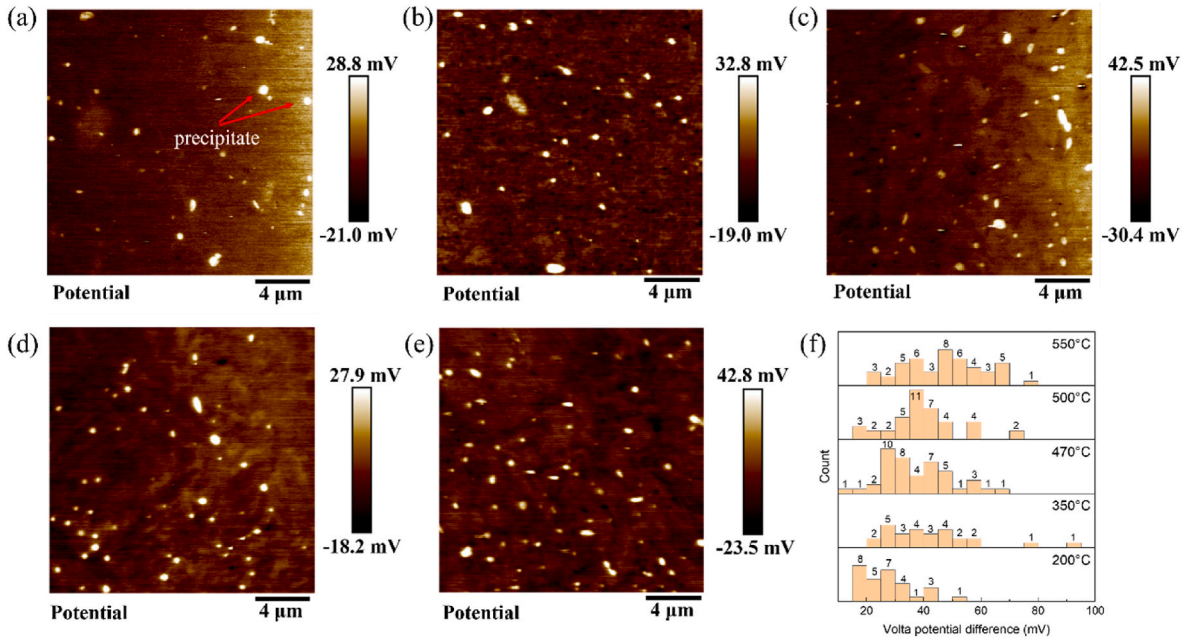

Fig. 4. SKPFM Volta potential maps of five different tempered samples: (a) 200 °C, (b) 350 °C, (c) 470 °C, (d) 500 °C, and (e) 550 °C; (f) the distribution of VPD between precipitates and the surrounding matrix within a 20 μm × 20 μm area.

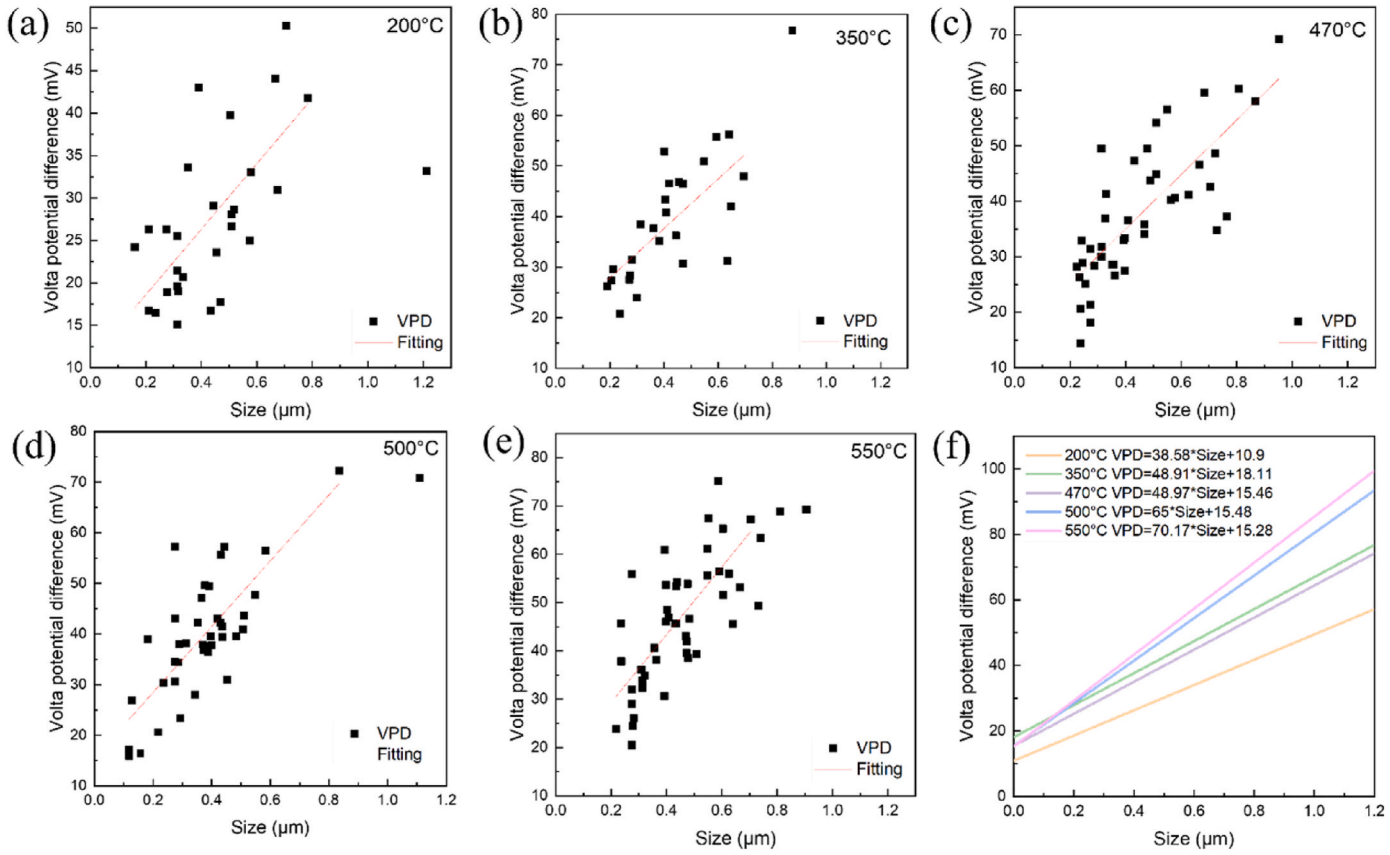

Fig. 5. The influence of precipitate size on the VPD for all samples: (a) 200 °C, (b) 350 °C, (c) 470 °C, (d) 500 °C, (e) 550 °C, and (f) fitting results.

stability of the passive film, and these locations are preferential sites for pit initiation [39,40].

In order to obtain a deeper understanding of the electrochemical behaviors involved in the HNMSS, cyclic voltammetry was employed to evaluate the influence of passive films formed on the different tempered HNMSS. Fig. 7a shows the CV curve of the sample tempered at 200 °C, which was scanned anodically from −1.2 to +0.6 V_{SCE} and then reversely scanned back to −1.2 V_{SCE}. The CV features shown in Fig. 7 are consistent with those reported in previous studies under similar experimental conditions [41]. The anodic peaks A1 and A2 correspond to the

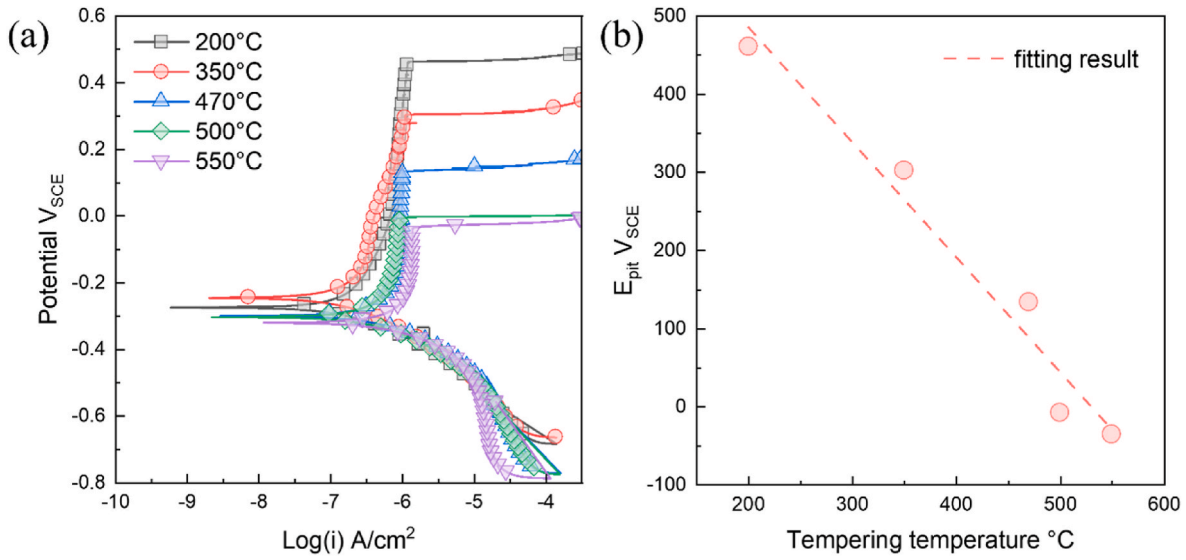

Fig. 6. Potentiodynamic polarization of HNMSS after tempering treatments: (a) potentiodynamic polarization curves; (b) pitting potential.

Table 2
Electrochemical parameters from potentiodynamic polarization measurements.

Temperature (°C)	E_{corr} (mV$_{SCE}$)	E_{pit} (mV$_{SCE}$)	i_p (μA/cm^2)
200	−271.92	461.28	0.836
350	−245.37	302.41	0.822
470	−298.73	133.72	0.977
500	−299.26	−35.88	0.914
550	−318.97	−8.09	1.333

oxidation of Fe to Fe^{2+} and the further oxidation of Fe^{2+} to Fe^{3+} (or Fe_2O_3), respectively. Notably, the anodic peak A3 corresponds to the oxidation of Cr_2O_3 to CrO_4^{2-} based on the CV results by Piao and Park [42]. The abrupt rise in current density above 0.5 V_{SCE} is attributed to the transpassive dissolution and oxygen evolution.

During the reverse scan after peak A3, cathodic peaks C2 and C1 emerge. Cathodic peak C2 is associated with the reduction of soluble oxidized species generated during the transpassive process, whereas cathodic peak C1 (−0.7 V_{SCE}) is related to the reduction of Fe_2O_3 to Fe^{2+}. The reduction peak of Cr^{6+} to Cr^{3+} reported at approximately 0 V_{SCE} was not detected in this study [43]. With the number of cycles increasing, the oxidation and reduction currents of the Fe^{2+}/Fe^{3+} increase gradually. However, only a distinct anodic peak A1 (−0.4 V_{SCE}) is observed for the 500 °C tempered sample, which shifts to a more positive potential and shows a higher peak current density than that of the 200 °C sample (−0.6 V_{SCE}). This indicates a stronger tendency toward depassivation of the high-temperature tempered sample. In addition, the cathodic peak C1 shifts from −0.7 to −0.6 V_{SCE} with a corresponding increase in cathodic current density, suggesting a reduced protective performance of the passive film.

To further clarify the thermodynamic reaction processes of HNMSS, the E–pH diagram of the Fe–Cr–N–H_2O system is shown in Fig. 7b. It is clearly observed that Fe under neutral conditions is progressively oxidized to Fe^{2+} and Fe_2O_3 as the applied potential increases, which is consistent with the CV results. For 200 °C tempered samples, CrN within the passive film may undergo the following reaction (Eq. (3)) at higher applied potentials to form Cr_2O_3 [12]. The transformation reaction can be calculated by the Pourbaix diagram in Fig. 6b. It is widely recognized

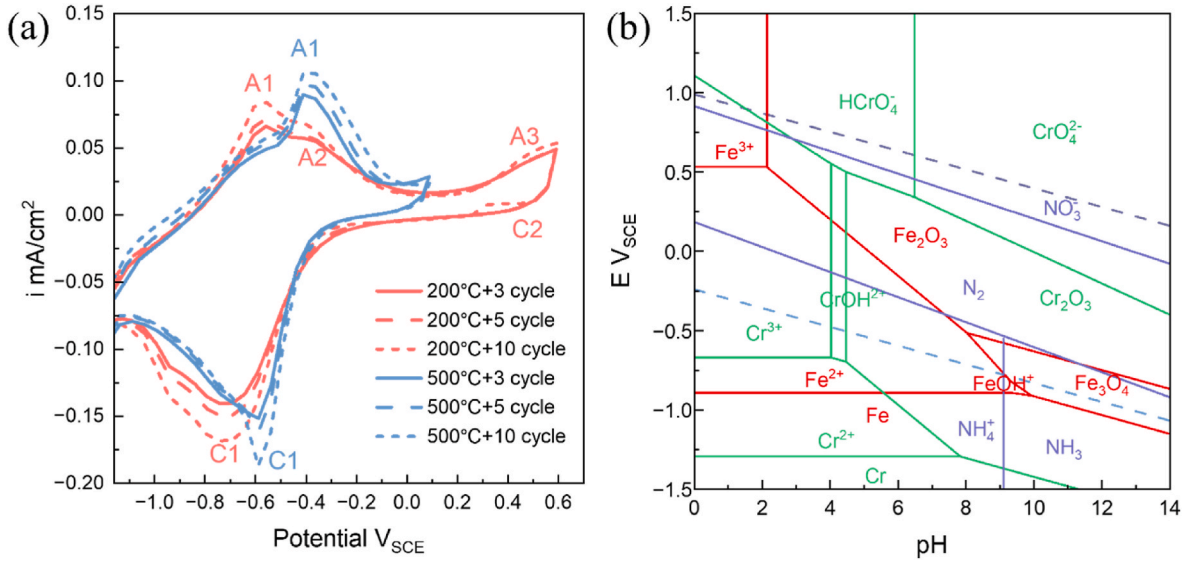

Fig. 7. (a) Cyclic voltammetry curves of 200 °C and 500 °C tempered samples in a 3.5 wt% NaCl solution; (b) Pourbaix diagram of the Fe–Cr–N–H_2O system at 25 °C and 1 atm.

that Cr_2O_3 is enriched in the passive film formed on the 200 °C sample.

$$2CrN + 3H_2O \rightarrow Cr_2O_3 + N_2 + 6H^+ + 6e \quad (3)$$

The corrosion manifests as distinct localized pitting in the temperature range of 200 °C to 500 °C, as observed from the corrosion morphologies in Fig. 8, with collapsed fringe cavities around the pits, and a small amount of uncorroded precipitates at the bottom of the pits. It is observed that the pit size grows from 23.74 to 78.14 μm as the tempering temperature increases (Fig. 8a–d), which reflects the weakening of the passive film. At a tempering temperature of 550 °C (Fig. 8e), the lath martensitic boundaries with numerous nano-/submicron carbides and nitrides become susceptible to corrosion, making them preferential sites for pitting. In contrast to the other four samples tempered at lower temperatures, the sample tempered at 550 °C exhibited corrosion across the entire specimen surface. This observation is similar to the corrosion morphology of 13 wt.% Cr martensitic stainless steel tempered at 550 °C after polarization testing [44].

According to the EDS mapping from Fig. 8f–i, it clearly shows severe corrosion occurring at the interface between the undissolved precipitates and the matrix. This indicates that the pitting resistance of HNMSS is related to the number of precipitates (M_2N and $M_{23}C_6$) and the extent of Cr depletion around these precipitates. Evidently, the amount of M_2N is greater than that of $M_{23}C_6$. The changes in the chemical composition of the interface region affect the stability of the passive film, enabling Cl^- to penetrate more easily, which renders these areas more susceptible to pitting corrosion. The decline of pitting resistance after a high tempering temperature is attributed to the formation of nano-scale Cr-rich carbides and nitrides along with the high density of Cr-depleted zones associated with the precipitates, which increases passive film inhomogeneity and results in the loss of passivity.

The EIS of the samples was measured to further evaluate the performance of the passive film on the sample surface. From the Nyquist plot shown in Fig. 9a, it can be observed that all tempered samples exhibit similar semicircles, which indicates that their corrosion mechanisms are not significantly affected by the tempering temperature. Generally, a larger radius of the capacitive arc results in better corrosion resistance. As the tempering temperature increases, the radius of the capacitive arc gradually decreases, which suggests that the corrosion resistance of the sample decreases with higher tempering temperatures.

Furthermore, the impedance modulus and phase angle (Fig. 9b) in the low-frequency range are the lowest when the tempering temperature reaches 550 °C, which indicates poorer stability of the passive film. Nevertheless, the experimental EIS data are fitted using the equivalent electric circuit depicted in Fig. 9a, which contains two time constants [37,45,46]. In the equivalent circuit, R_s represents the solution resistance. In the first time constant, the constant phase element CPE_1 is attributed to the electrochemical behavior of the outer layer and the electrical double layer formed at the passive film/solution interface [47]. The resistance R_1 is related to the diffusion resistance along the ionic migration pathways. In the second time constant, CPE_2 reflects the electrochemical response of the barrier layer, which is a highly point-defective layer at the end of the channel defects [48]. R_2 represents the charge transfer resistance, which is likely to correspond to reactions that occur at defect sites in the passive film or at the inner oxide/substrate interface [49,50]. The impedance of the CPE can be calculated using the following equation [51,52]:

$$Z(CPE) = Q^{-1}(j\omega)^{-\alpha} \quad (3)$$

where Q denotes the CPE parameter, j is $\sqrt{-1}$, ω denotes the angular frequency, and α is the dispersion coefficient related to surface inhomogeneity.

The interface reaction rate is determined by the polarization resistance R_p, defined as $R_p = R_1 + R_2$, which represents the corrosion resistance of the metal. The fitting results are listed in Table 3. Among them, the sample at 200 °C exhibits the highest polarization resistance, with a value of approximately 1.73×10^5 Ω cm^2. Contrastingly, the

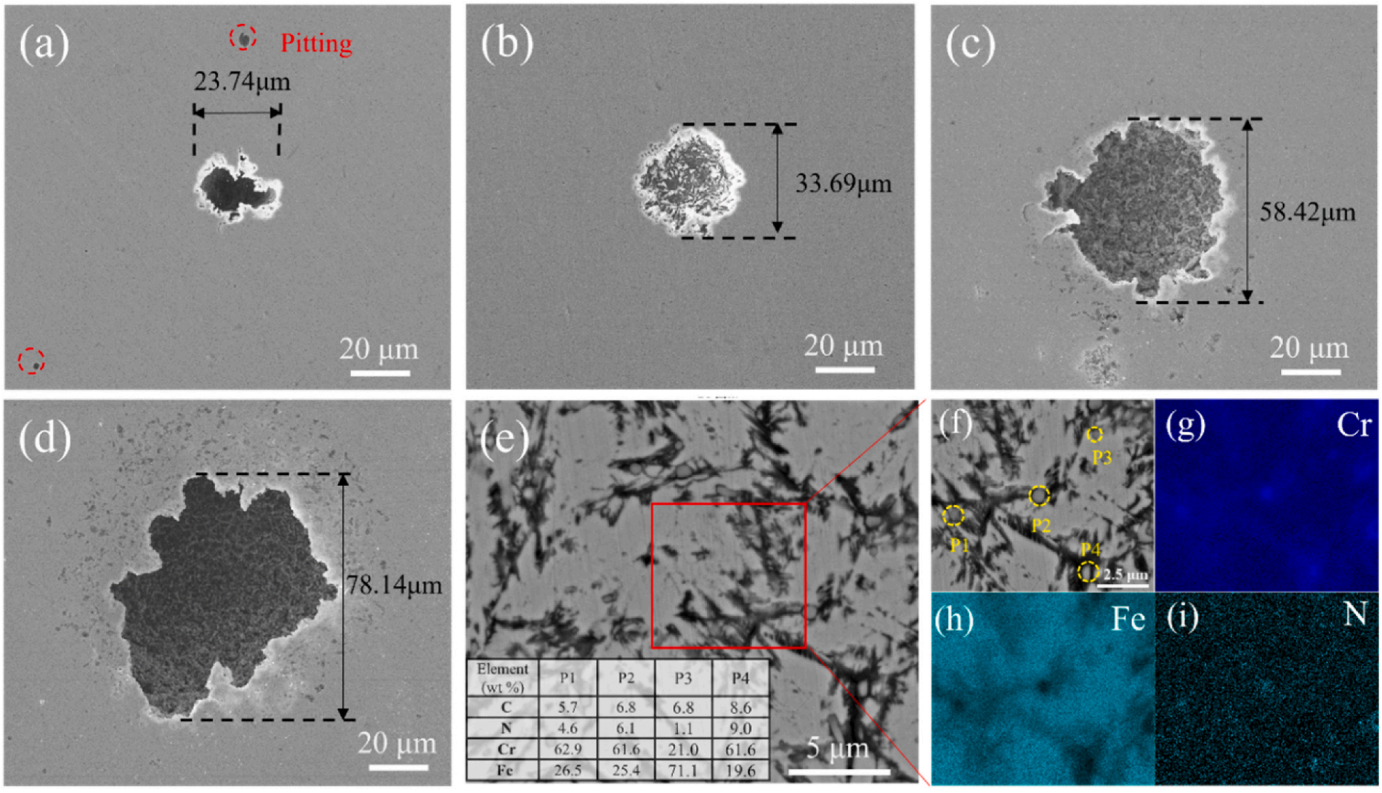

Element (wt %)	P1	P2	P3	P4
C	5.7	6.8	6.8	8.6
N	4.6	6.1	1.1	9.0
Cr	62.9	61.6	21.0	61.6
Fe	26.5	25.4	71.1	19.6

Fig. 8. Corrosion morphologies of the specimen after the polarization test. (a) 200 °C, (b) 350 °C, (c) 470 °C, (d) 500 °C, (e) 550 °C, (f–i) high magnification SEM image and EDS element mapping in (e). P1, P2, P4 corresponds to M_2N, and P3 corresponds to $M_{23}C_6$.

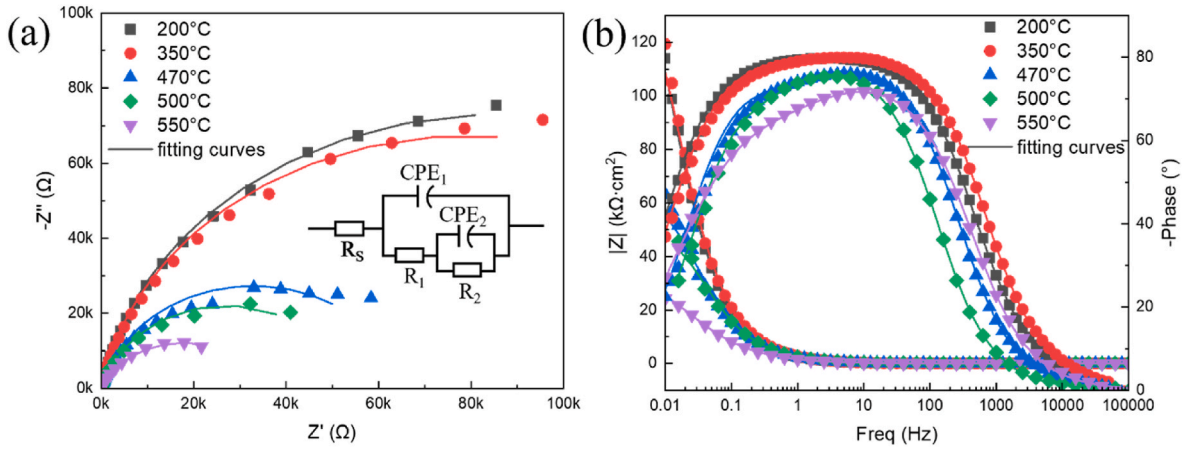

Fig. 9. EIS plots of the different tempering HNMSS: (a) Nyquist plots, (b) Bode plots.

polarization resistance of the sample at 550 °C is only $3.62 \times 10^4\ \Omega\ cm^2$, which is more than a fourfold decrease compared to the 200 °C sample. This reduction is primarily attributed to the precipitation and coarsening of a large number of Cr-rich carbides and nitrides under high-temperature tempering conditions, resulting in the formation of Cr-depleted zones around the matrix and the reduced participation of N in passivation, which decreases the stability of the passive film and thus reduces the corrosion resistance of the high-temperature tempered sample.

3.4. Quasi-in-situ EBSD and SKPFM measurements

Quasi-*in-situ* EBSD and SKPFM measurements were further performed to explain the influence of complex microstructures (martensitic matrix, RA, and Cr-rich precipitates) on the corrosion resistance of HNMSS. Fig. 10a and b show the IPF and phase distribution of the specimen tempered at 200 °C. The blue regions represent HCP M_2N (Cr_2N, $P\bar{3}\ 1\ m$, a = b = 4.8, c = 4.4462, ICSD 4311894), green areas correspond to FCC RA, yellow refers to FCC $M_{23}C_6$ carbides ($Cr_{23}C_6$, Fm $\bar{3}$ m, a = b = c = 10.6595, ICSD 62667), and red represents martensite.

The M_2N and $M_{23}C_6$ precipitates are primarily located at the interfaces between lath martensite and RA, as well as within the RA grains. According to the EDS results shown in Fig. 10c–i, the submicron-sized precipitates are mainly M_2N (highlighted in blue circles), with minor amounts of $M_{23}C_6$ (highlighted in green circles). SKPFM tests were employed to characterize the surface morphology and corresponding Volta potential (Fig. 10j and k). Fig. 10l illustrates the Volta potential between the M_2N precipitates and the martensitic/RA matrix. It can be observed that the M_2N precipitates exhibit a higher Volta potential than the matrix, which acts as a cathodic phase. Concurrently, the Volta potential of RA is higher than that of martensite, which indicates that RA has a more stable passive film and a beneficial effect on the corrosion resistance [53]. The presence of both blocky and film RA greatly reduces the VPDs between the precipitates and the matrix, thereby decreasing the galvanic corrosion effect.

The relationship between the different sizes of M_2N precipitates and their VPD is further analyzed in Fig. 11a, which reveals an apparent size effect on the measured Volta potential for the sample tempered at 200 °C [36]. Clearly, as the size of the M_2N precipitate increases, the precipitate still exists as a cathode whose VPD exhibits an increasing trend, and the maximum VPD between M_2N and martensitic can reach nearly 25.96 mV. Moreover, the presence of RA reduces the VPD between the M_2N precipitate and the matrix, the maximum reduction of which is approximately 15.55 mV. Meanwhile, DFT calculations were performed to determine the work functions of various phases. Based on the IPF of Fig. 10a shown in Fig. 11b, it is evident that the orientations of RA, martensitic matrix, M_2N, and $M_{23}C_6$ phases are close to the (101), (001), (0001), and (001) planes, respectively. The calculated work functions of RA, martensitic matrix, M_2N, and $M_{23}C_6$ phases are 4.60, 3.97, 5.34, and 4.53 eV (Fig. 11c). The averaged vacuum potential and Fermi level are presented in Supplementary Fig. S1 and Table S1.

Fundamentally, the work function determines the minimum energy required to remove an electron from the corresponding surface [54,55], and a lower work function implies a higher probability of losing electrons and a higher tendency of corrosion. Consequently, it can be concluded that M_2N has the highest work function, serving as a cathodic phase that is not prone to corrosion. The RA exhibits a higher work function compared to the martensitic, which reduces the potential difference, conforming to the SKPFM observations.

Furthermore, the effect of microstructural evolution after high-temperature tempering at 550 °C on the corrosion resistance of HNMSS was investigated (Fig. 12). It can be observed that RA has completely disappeared, and the primary submicron-sized precipitates remain as M_2N based on the IPF and phase distribution (Fig. 12a and b). As shown in Fig. 12c–h, the M_2N precipitates in the sample tempered at 550 °C are still rich in Cr, C, and N. According to the SKPFM results presented in Fig. 12i and j, M_2N consistently exhibits a higher Volta potential than the surrounding martensitic matrix. The VPD between M_2N and martensite reaches a maximum of 35.09 mV (Fig. 12k and l). All results denote that the reduced percentage of RA at high temperatures results in a greater VPD compared to the samples tempered at a low temperature, which has a significantly accelerated galvanic corrosion. The M_2N precipitates act as a cathode exposed to a corrosive environment, while the surrounding matrix acts as the anode undergoing

Table 3
Fitted parameters of the EIS spectra.

Temp. (°C)	R_s ($\Omega\cdot cm^2$)	CPE_1 ($s^n/\Omega\ cm^2$)	n_1	R_1 ($\Omega\cdot cm^2$)	CPE_2 ($s^n/\Omega\ cm^2$)	n_2	R_2 ($\Omega\cdot cm^2$)	R_p ($\Omega\cdot cm^2$)
200	9.60	6.90×10^{-5}	0.88	1.46×10^5	3.94×10^{-6}	0.90	2.70×10^4	1.73×10^5
350	7.11	7.10×10^{-5}	0.89	1.40×10^5	6.65×10^{-6}	0.93	2.73×10^4	1.68×10^5
470	8.52	7.90×10^{-5}	0.88	2.30×10^4	2.50×10^{-5}	0.94	4.23×10^4	6.53×10^4
500	9.53	7.41×10^{-5}	0.89	2.39×10^4	4.21×10^{-5}	0.92	2.91×10^4	5.30×10^4
550	10.47	1.19×10^{-4}	0.85	5.08×10^3	6.74×10^{-5}	0.64	3.11×10^4	3.62×10^4

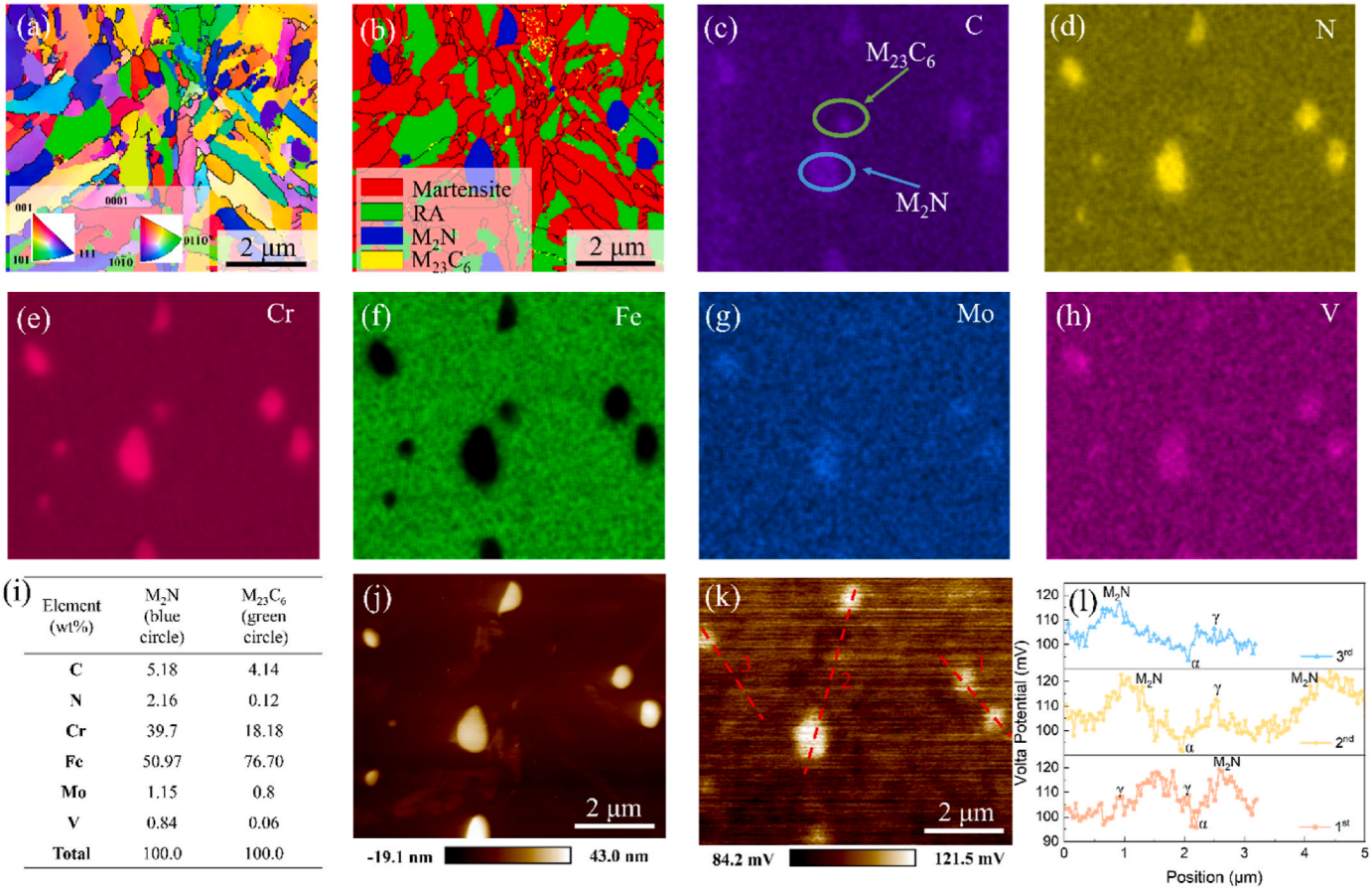

Fig. 10. High-magnification results of the sample tempered at 200 °C. The (a) IPF and (b) phase map of EBSD; (c–h) EDS element mapping; (i) Chemical compositions of marked precipitates by EDS in (c); SKPFM detected (j) surface height, (k) Volta potential, and (l) Volta potential of a line as indicated in (k).

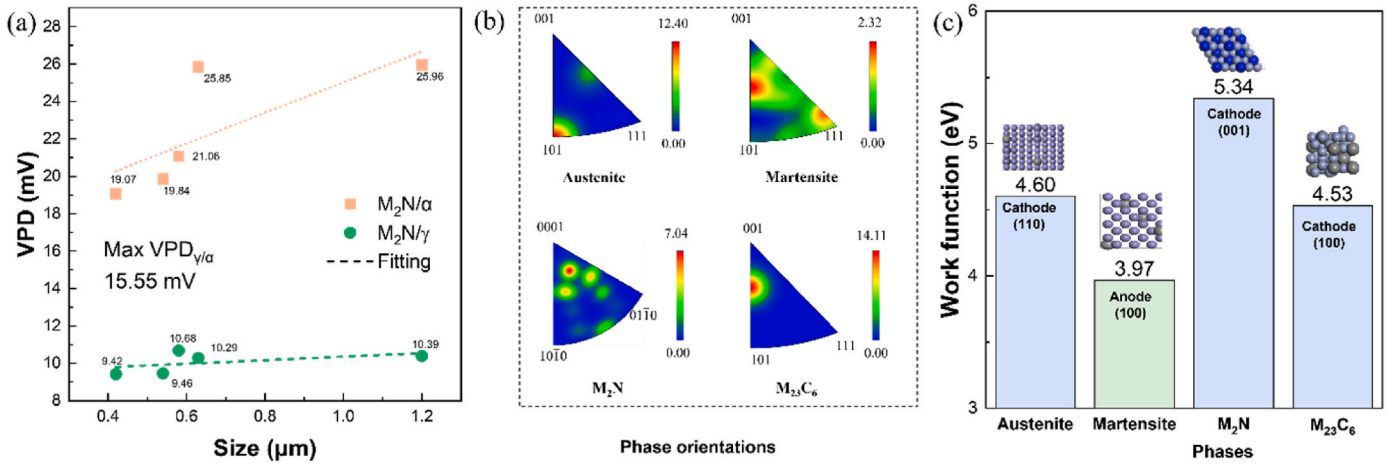

Fig. 11. VPD-size effect of M_2N precipitates tempered at 200 °C: (a) VPD of a line as indicated in Fig. 10k; (b) IPF of HNMSS that corresponds to the orientation map; (c) work functions calculated by DFT.

dissolution [56]. This phenomenon provides a reasonable explanation for the corrosion morphology observed in Fig. 8e.

3.5. Semiconductor properties and XPS measurements of the passive film

Based on the electrochemical and SEM results, the corrosion resistance gradually decreases as the tempering temperature increases. The formation of stable pitting is related to the stability of the passive film. Potentiostatic polarization at 0.1 V_{SCE} was performed on all samples in 3.5 wt.% NaCl solution for 1 h (Fig. 13) to better understand the transition from metastable to stable pitting in the tempered samples. Each anodic current spike represents the formation of a metastable pit, which corresponds to the nucleation and repassivation of metastable pits [57–59]. At a tempering temperature of 200 °C and 350 °C, fewer current transients are observed. As the tempering temperature increases, the frequency of metastable pit events increases, particularly for the

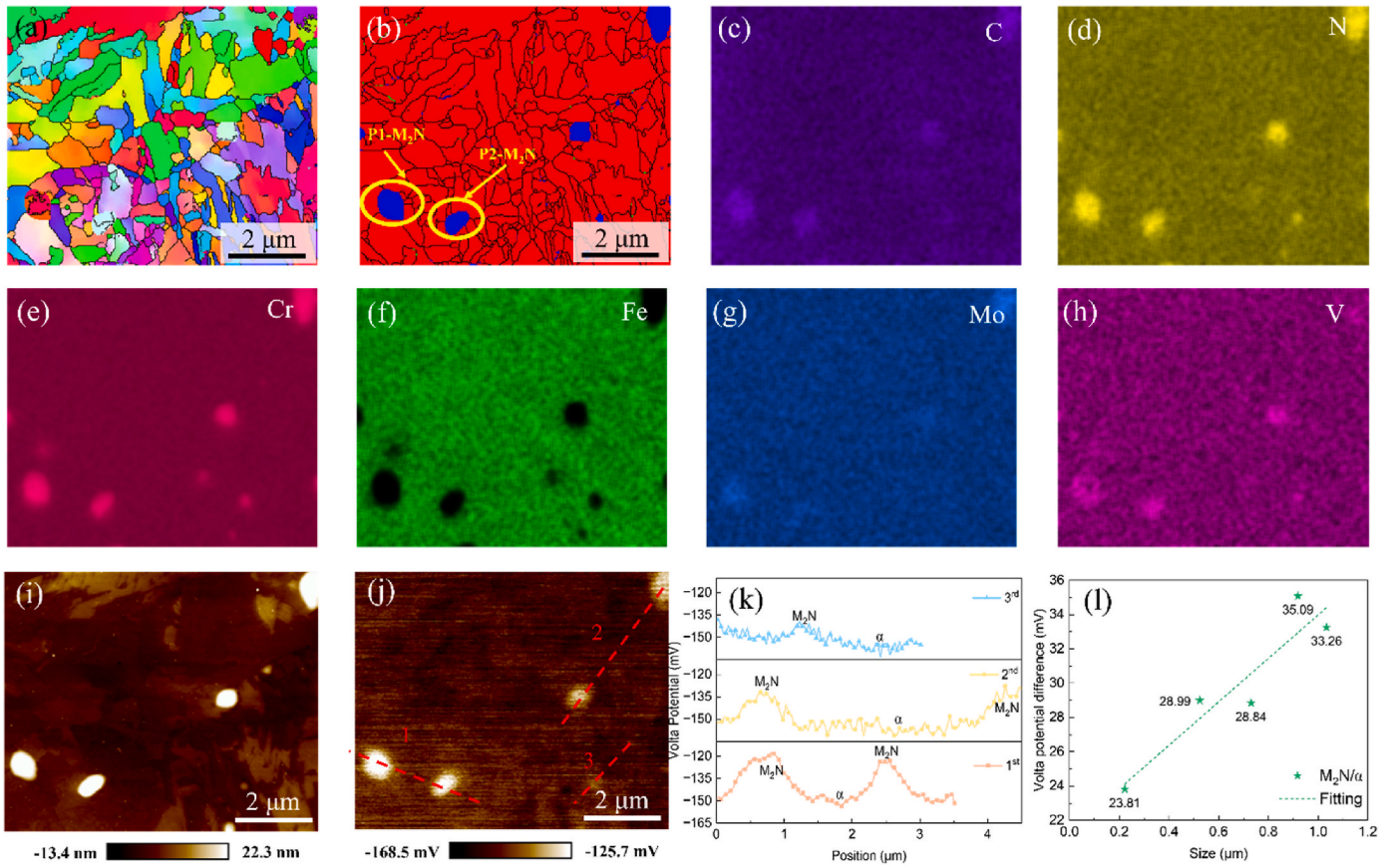

Fig. 12. High-magnification results of the sample tempered at 550 °C. (a) IPF of EBSD; (b) phase map of EBSD; (c–h) EDS element mapping; (i) surface topography and (j) Volta potential of SKPFM; (k) Volta potential of a line as indicated in (j); (l) VPD between M_2N and the matrix.

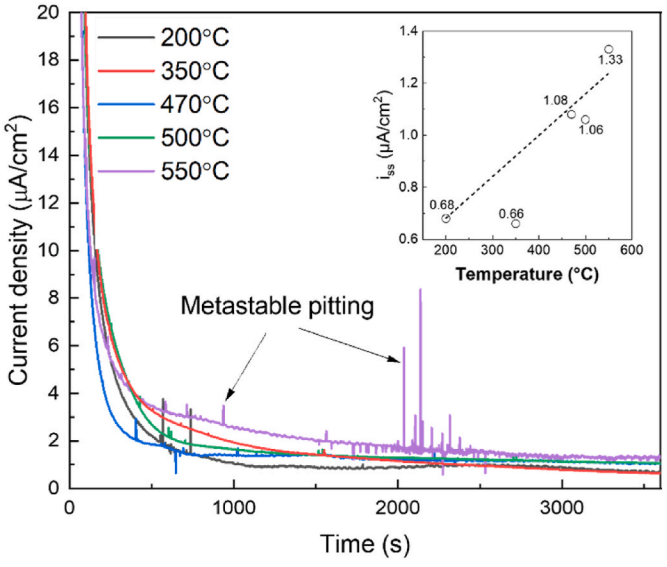

Fig. 13. Typical current–time curves of the specimens tempered at different temperatures conducted in 3.5 wt % NaCl solution at −0.1 V_{SCE}.

sample tempered at 550 °C, and the steady-state current density (i_{ss}) greatly improves. The increase in i_{ss} suggests that the concentration of defects in the passive film increases [60]. The frequency of metastable pitting events exhibits an increasing trend as the RA content decreases. The increased potential difference between the precipitates and the matrix significantly promotes the pitting susceptibility.

The semiconductor properties of passive films were determined from the variation in interfacial capacitance of the passive film and the Helmholtz layer with the applied potential. The Mott–Schottky relation describing the dependence of the space charge capacitance (C_{sc}) on the applied potential V is expressed as [61,62]:

$$\frac{1}{C_{sc}^2} = \pm \frac{2}{\varepsilon\varepsilon_0 eNA^2}\left(V - V_{FB} - \frac{k_B T}{e}\right) \quad (4)$$

where the positive sign is for an n–type semiconductor and the negative sign is for a p–type semiconductor, donor density (N_D) for n-type or acceptor density (N_A) for p-type semiconductors, e is the electron charge (1.602×10^{-19}C), ε is the relative dielectric constant of the semiconductor, ε_0 is the vacuum permittivity (8.854×10^{-14} F/cm), A is the surface area of the working electrode (1 cm^2), k_B is Boltzmann constant (1.38×10^{-23} J/K), T represents absolute temperature, V is the applied potential and V_{FB} represents the flat band potential.

The positive slope of C_{sc}^{-2} vs. V in Fig. 14a illustrates that the passive film formed on the HNMSS after various heat treatments and characterized under potentiostatic polarization at −0.1 V_{SCE} in a 3.5 wt% NaCl solution exhibits n-type semiconductor properties, which are mainly dominated by iron oxides and hydroxides [63,64]. The donor density (N_D) can be calculated from the slope of the linear region in the Mott–Schottky plot. The N_D values for the samples tempered at 200, 350, 470, 500, and 550 °C are 1.45×10^{21} cm^{-3},1.64×10^{21} cm^{-3}, 1.77×10^{21} cm^{-3}, 1.78×10^{21} cm^{-3}, and 2.36×10^{21} cm^{-3} in Fig. 14b, respectively. According to the point defect model (PDM), the passive film behaves as an n-type semiconductor for the HNMSS, in which O vacancies and cation interstitials are identified as the primary intrinsic defects [65]. At the same time, passivity breakdown tends to initiate at surface sites characterized by high vacancy diffusivity, including the

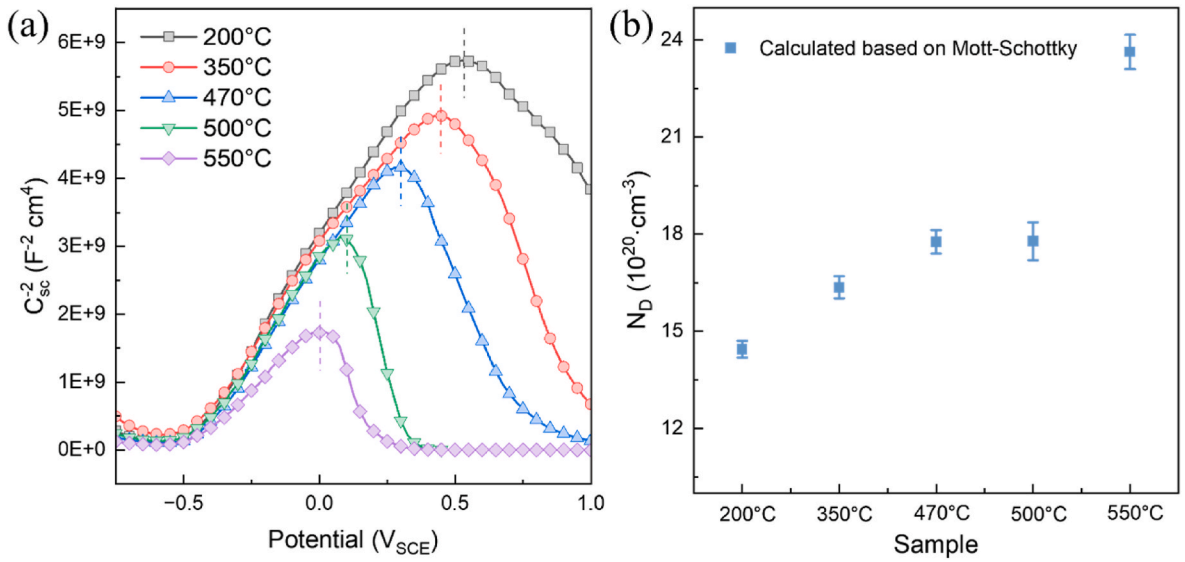

Fig. 14. Mott-Schottky plots of the (a) different tempered HNMSS; (b) the calculated variation of donor densities (N_D).

interfacial boundaries between precipitates and the matrix. The rise in donor density (N_D) under high-temperature tempering conditions indicates a progressive acceleration in the dissolution rate of the passive film.

To reveal the compositional variations of the passive films formed on samples tempered at different temperatures, XPS analyses were conducted after potentiostatic polarization at −0.1 V_{SCE} for 1 h. The peaks of Cr, Fe, O, and N are identified in the XPS full energy survey for each tempering temperature to examine the composition of the passive film (Supplementary Fig. S2). Fig. 15a–d presents the XPS results for Cr, Fe, O, and N elements in the passive film. The five samples exhibit similar peaks, which indicates that the composition of the passive film is essentially consistent across all samples.

Cr 2p3/2 spectra peaks can be identified as metallic Cr^0 (574.2 eV), CrN (575.7 eV), Cr_2O_3 (576.1 eV), and $Cr(OH)_3$ (578.1 eV). In a previous study, Zhang et al. [66] proved the existence of these components in 3.5 wt% NaCl solution for high nitrogen stainless steel. In Fig. 16a, the sample tempered at 200 °C has the highest ratio of Cr oxide and Cr hydroxide (Cr_{ox}/Cr_{hy}), reaching 4.82. As the tempering temperature increases, the Cr_{ox}/Cr_{hy} ratio gradually decreases, reaching its lowest value of 2.1 at 550 °C. Previous studies have shown that the higher the percentage of hydroxide in the passive film, the worse the corrosion resistance [67,68]. This is owing to the substantial precipitation of Cr-rich nitrides, which reduces the N content in the matrix, making it less favorable for Cr_2O_3 enrichment in the passive film [67,69]. Additionally, Cr_2O_3 has greater thermodynamic stability and a lower concentration of point defects compared to $Cr(OH)_3$, which enhances the stability of the passive film [70].

Furthermore, Fe 2p3/2 spectra are comprised of Fe^0 (706.7 eV), FeO (709.5 eV), Fe_2O_3 (710.3 eV), and FeOOH (712.3 eV). A fraction of Fe_{ox+hy}/Cr_{ox+hy} was obtained and shown in Fig. 16a. As the tempering temperature increases, Fe oxides and hydroxides become the main components in the passive film, particularly for the sample tempered at 550 °C. Meanwhile, its defect concentration is the highest among all tempering temperatures. Chen et al. [71] reported that an increase in the Fe_{ox+hy}/Cr_{ox+hy} resulted in a less protective passive film, primarily owing to a decrease in the Cr content of the outer layer of the passive film.

Regarding N, its forms in the passive film are N^0 (397.2 eV), NH_3 (399.5 eV), and NH_4^+ (400.3 eV). Sun et al. [72] reported that NH_3 adsorption on the stainless steel surface can enhance the stability of the passive film. N dissolved in the matrix primarily exists as CrN, which can consume H^+ in the solution to form NH_4^+ according to Eq. (5) [73]:

$$2CrN + 3H_2O \rightarrow Cr_2O_3 + 2NH_3 \quad (5)$$

Meanwhile, the N in the matrix will also consume H^+ to promote the formation of NH_3 and NH_4^+ in the film layer, as indicated in Eqs. (6) and (7), thereby increasing the local pH value [11,74]. This process hinders the self-catalytic reactions and promotes the repassivation process of metastable pitting. In Fig. 16b and c, the sum of NH_4^+ and NH_3 in the passive film of the sample tempered at 200 °C is highest. A higher N content in the matrix effectively inhibits the occurrence of pitting corrosion [13].

$$[N] + 3H^+ + 3e^- \rightarrow NH_3 \quad (6)$$

$$[N] + 4H^+ + 3e^- \rightarrow NH_4^+ \quad (7)$$

The O element in the passive film is composed of O^{2-} (530.2 eV), OH^- (532 eV), and H_2O (533.6 eV). From Fig. 16a, it can be observed that the O^{2-}/OH^- ratios at tempering temperatures of 200 °C, 350 °C, 470 °C, 500 °C, and 550 °C are 0.76, 0.83, 0.44, 0.55, and 0.5, respectively. Notably, the O^{2-}/OH^- ratio decreases significantly at higher tempering temperatures, which accelerates corrosion [75]. Based on electrochemical results, the corrosion resistance gradually decreases as the tempering temperature increases from 200 °C to 550 °C. The decrease in corrosion resistance is related to the degradation of the passive film according to the XPS results.

3.6. Mechanistic insights into corrosion resistance of HNMSS

To obtain deeper insight into the extensive loss of passivation observed in the high-temperature tempered sample, the 550 °C tempered specimen was examined by TEM in Fig. 17. For the 550 °C sample, the bright-field and dark-field TEM images (Fig. 17a–c) reveal that a large number of fine needle-like nanosized precipitates (approximately 10–30 nm) are scattered within the grains, and present at the lath martensite interfaces, which these nanosized precipitates are formed during the secondary hardening stage.

The Fast Fourier Transform (FFT) pattern shown in Fig. 17d indicates that the d-values of the three directions are 4.147 Å, 2.006 Å, and 2.371 Å, which can be further indexed as the planes of (10 $\bar{1}$ 0), (10$\bar{1}$ 1), and ($\bar{1}$ 2$\bar{1}$ 0) for HCP M_2N nitride. Additionally, the orientation relationship between the martensite and M_2N is (11 $\bar{1}$) α//(0001) M_2N and [011] α//[10 $\bar{1}$ 0] M_2N. At the same time, the corresponding EDS mapping results for HCP M_2N nitride are shown in Fig. 17e–h. It is worth noting

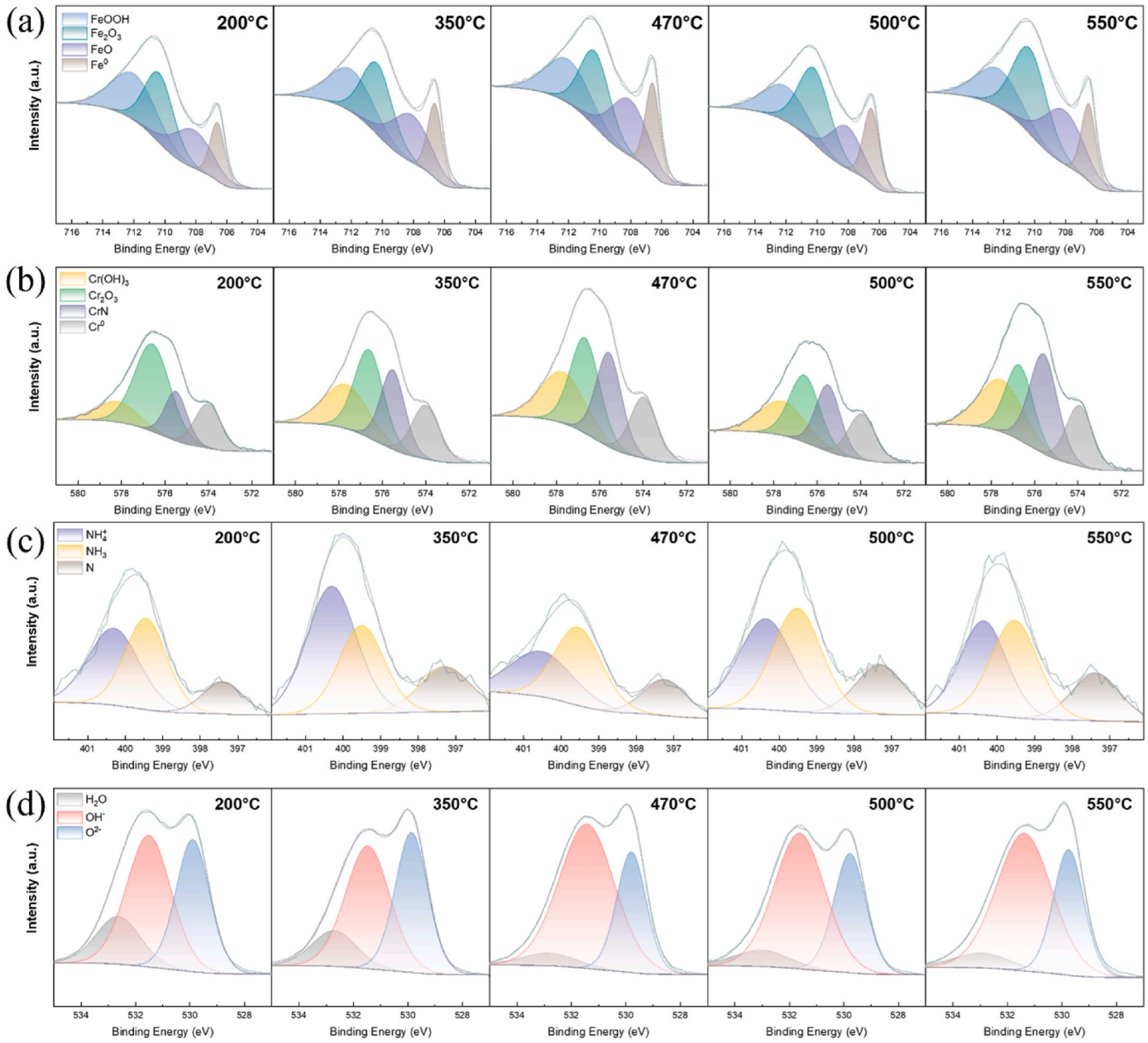

Fig. 15. XPS results of passive films on the different tempered samples in 3.5 wt% NaCl. (a) Fe 2p3/2; (b) Cr 2p3/2; (c) N 1s; (d) O 1s.

that the nanoscale precipitates formed in the martensitic matrix after high-temperature tempering further increase the compositional and structural inhomogeneity of the passive film, as the passive film formed on the M_2N precipitates exhibits a higher Cr_2O_3 content compared with that formed on the martensitic matrix.

The corrosion process shown in Fig. 18 is proposed based on the preceding analysis. At lower tempering temperatures, N in the matrix, as an austenite-stabilizing element, can enhance the pitting corrosion resistance of HNMSS. This is primarily because the N dissolved in the matrix exists primarily in the form of CrN in the passive film (XPS results). CrN can consume H^+ ions in the solution, thereby hindering the autocatalytic process and promoting the repassivation of metastable pits. As the tempering temperature increases, N precipitates from the matrix to form M_2N, and the lower Cr content in the matrix hinders the enrichment of Cr_2O_3 and $Cr(OH)_3$ in the passive film, which decreases in its corrosion resistance. According to DFT calculations, M_2N has the highest work function, indicating greater electrochemical inertness. The increased potential difference between M_2N and the matrix leads to rapid dissolution of the surrounding matrix and accelerates corrosion, while the precipitates remain unaffected. Moreover, the substantial precipitation of Cr-rich nitrides reduces Cr and N in the substrate and a marked depletion of Cr in the surface region when tempered at 550 °C. The lack of Cr limits the formation of passive films at the interface between the precipitates and the matrix, which further promotes the initiation and propagation of localized corrosion.

4. Conclusions

The influence of different tempering temperatures (200 °C, 350 °C, 470 °C, 500 °C, and 550 °C) on passive film and its effect on the corrosion behavior of HNMSS was systematically studied. Based on experimental observations and DFT calculations, the following conclusions are drawn.

1) Precipitate size strongly affects the measured Volta potential by SKPFM. The high-temperature tempered samples show a greater

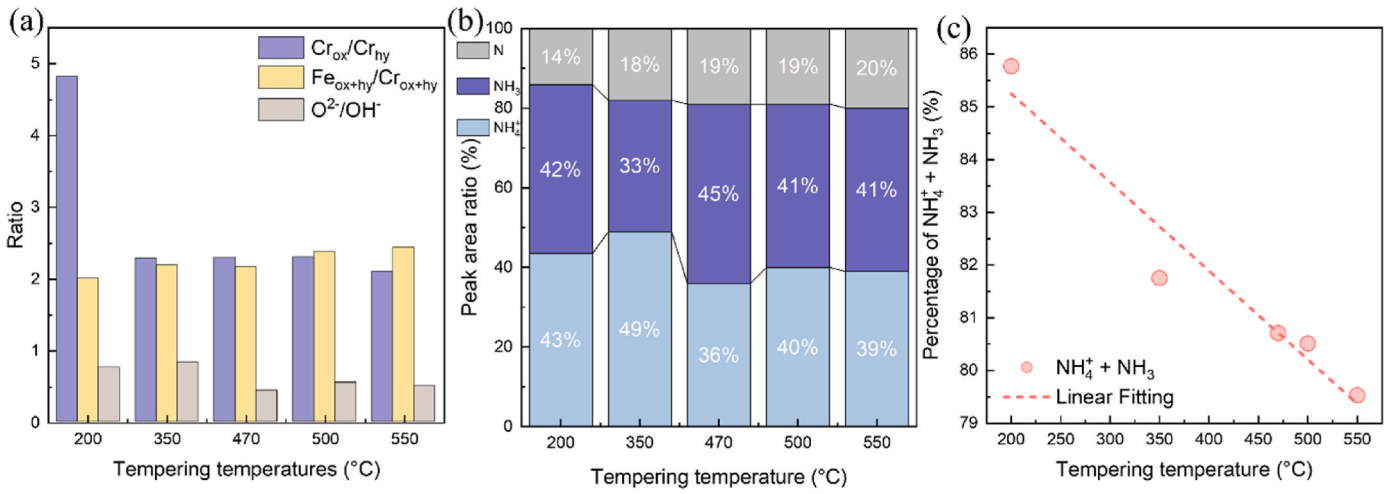

Fig. 16. Compositional ratios in passive films of different tempering samples. (a) Cr_{ox}/Cr_{hy}, Fe_{ox+hy}/Cr_{ox+hy}, and O^{2-}/OH^{-}, (b) NH+ 4 and NH_3, (c) fitting result.

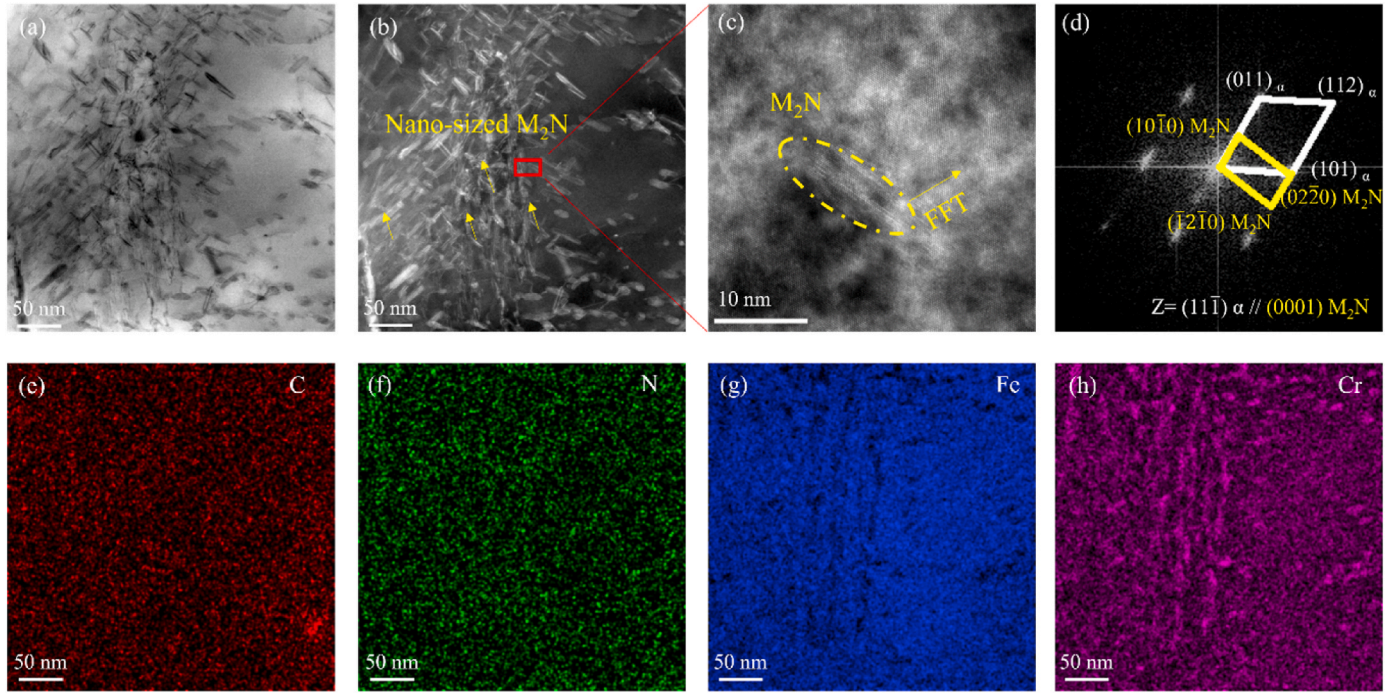

Fig. 17. TEM micrographs of HNMSS tempering at 550 °C. (a) bright-field image; (b) dark-field image; (c) HRTEM morphology and (d) FFT pattern of nanosized precipitate in (c); (e–h) the elemental distribution maps.

sensitivity of the potential difference to precipitate size than those tempered at lower temperatures. Notably, the potential difference between 1 μm precipitates and the matrix reaches approximately 70 mV in the 550 °C sample.

2) As the tempering temperature increases, the electrochemical corrosion performance of tempered HNMSS deteriorates, and the frequency of metastable pitting increases, which results in higher the pitting sensitivity. Specifically, their pitting potentials significantly decrease from 461.28 mV_{SCE} (200 °C) to −8.09 mV_{SCE} (550 °C), and the protective performance of the passive film was weakened by 79%. The passive film formed on HNMSS is dominated by oxygen vacancies and cation interstitials, resulting in n-type semiconducting behavior. The donor density (N_D) gradually increases, which promotes the adsorption and enrichment of Cl^- at these defect sites.
3) Based on DFT calculations, the sequence of structural work functions in the HNMSS is as follows: M_2N > RA > $M_{23}C_6$> Martensitic. The SKPFM results confirm that the M_2N precipitate acts as a cathode in corrosion reaction, and that their VPDs with the matrix exhibit an increasing trend as the size of the M_2N precipitate increases. The Volta potential of the RA is approximately 15.55 mV higher than that of martensite.
4) As the tempering temperature increases, N is sequestered within the cathode phase as M_2N, thereby precluding its substantial release from the matrix to partake in the formation of the passive film. XPS results confirm that the formation of ammonium on the surface and the reduction of Cr content within the passive film, particularly Cr_2O_3 and CrN, diminish the corrosion resistance of the HNMSS.

Author contributions

X.F. performed the experiment verification and wrote the manuscript. Y.J., C.L. and W.Q. conceptualized the project and carried out

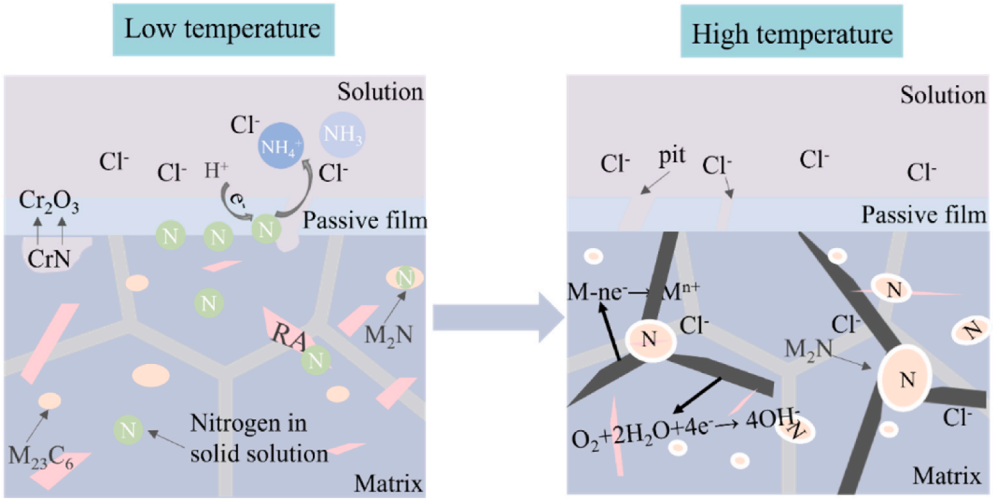

Fig. 18. Schematic of the corrosion mechanism of HNMSS at different tempering temperatures.

DFT calculations. C.W. and W.C. prepared the materials. P.D., X.C., J.L., and C.D. analyzed the experiment data and edited the manuscript. J.L. and C.D. helped fine-tune the project and revised the manuscript.

Declaration of competing interest

The authors declare that they have no known competing financial interests or personal relationships that could have appeared to influence the work reported in this paper.

Acknowledgements

This research was supported by the National Natural Science Foundation of China (No. 52125102), the China Postdoctoral Science Foundation (No. 2024M750172), and the Young Elite Scientists Sponsorship Program by CAST (YESS20240240). This work was sponsored by Nederlandse Organisatie voor WetenschappelijkOnderzoek (The Netherlands Organization for Scientific Research, NWO) domain Science for the use of supercomputer facilities.

Appendix A. Supplementary data

Supplementary data to this article can be found online at https://doi.org/10.1016/j.jmrt.2026.02.120.

Data availability

The data that support the findings of this study are available from the corresponding author upon reasonable request.

References

[1] Li Fuyang, Tian Jialong, Li Huabing, Deineko LM, Jiang Zhouhua. Simultaneously enhancing strength, ductility and corrosion resistance of a martensitic stainless steel via substituting carbon by nitrogen. Acta Metall Sin 2023;36:705–16.
[2] Kamachi Mudali U, Khatak HS, Raj Baldev, Uhlemann M. Surface alloying of nitrogen to improve corrosion resistance of steels and stainless steels. Mater Manuf Processes 2004;19:61–73.
[3] Averbach BL, Lou Bingzhe, Pearson PK, Fairchild RE, Bamberger EN. Fatigue crack propagation in carburized high alloy bearing steels. Metall Trans A 1985;16:1253–65.
[4] Berns Hans, Gavriljuk Valentin, Shanina Bela. Intensive interstitial strengthening of stainless steels. Adv Eng Mater 2008;10:1083–93.
[5] Fan Ruicheng, Gao Ming, Ma Yingche, Zha Xiangdong, Xianchao Hao, Liu Kui. Effects of heat treatment and nitrogen on microstructure and mechanical properties of 1Cr12NiMo martensitic stainless steel. J Mater Sci Technol 2012;28:1059–66.
[6] Jiang Zhouhua, Feng Hao, Li Huabing, Zhu Hongchun, Zhang Shucai, Zhang Binbin, et al. Relationship between microstructure and corrosion behavior of martensitic high nitrogen stainless steel 30Cr15Mo1N at different austenitizing temperatures. Materials 2017;10.
[7] Wang LJ, Sheng LY, Hong CM. Influence of grain boundary carbides on mechanical properties of high nitrogen austenitic stainless steel. Mater Des 2012;37:349–55.
[8] Wang Rui, Li Fenghao, Yu Zhiqiang, Kang Yan, Li Meng, Hu Yong, et al. Influences of partial substitution of C by N on the microstructure and mechanical properties of 9Cr18Mo martensitic stainless steel. Mater Des 2023;236:112497.
[9] Qin Yu, Li Juan, Herbig Michael. Microstructural origin of the outstanding durability of the high nitrogen bearing steel X30CrMoN15-1. Mater Charact 2020;159:110049.
[10] Toro Alejandro, Wojciech Z. Misiolek, André Paulo Tschiptschin, Correlations between microstructure and surface properties in a high nitrogen martensitic stainless steel. Acta Mater 2003;51:3363–74.
[11] Ha HeonYoung, Jang HeeJin, Kwon HyukSang, Kim SungJoon. Effects of nitrogen on the passivity of Fe–20Cr alloy. Corros Sci 2009;51:48–53.
[12] Yue Xiaoqi, Alfred Larsson, Tang Huajie, Grespi Andrea, Scardamaglia Mattia, Shavorskiy Andrey, et al. Synchrotron-based near ambient-pressure X-ray photoelectron spectroscopy and electrochemical studies of passivation behavior of N- and V-containing martensitic stainless steel. Corros Sci 2023;214:111018.
[13] Gao Fengyin, Qiao Yanxin, Chen Jian, Yang Lanlan, Zhou Huiling, Zheng Zhibin, et al. Effect of nitrogen content on corrosion behavior of high-nitrogen austenitic stainless steel. npj Mater Degrad 2023;7:75.
[14] Cheng Hongxu, Luo Hong, Wang Xuefei, Pan Zhimin, Jiang Yi, Li Xiaogang. Electrochemical corrosion and passive behavior of a new high-nitrogen austenitic stainless steel in chloride environment. Mater Chem Phys 2022;292:126837.
[15] Jiao Wei-Chao, Li Hua-Bing, Dai Jing, Feng Hao, Jiang Zhou-Hua, Zhang Tao, et al. Effect of partial replacement of carbon by nitrogen on intergranular corrosion behavior of high nitrogen martensitic stainless steels. J Mater Sci Technol 2019;35:2357–64.
[16] Chen Dihao, Dong Chaofang, Ma Yuan, Ji Yucheng, Gao Lei, Li Xiaogang. Revealing the inner rules of PREN from electronic aspect by first-principles calculations. Corros Sci 2021;189:109561.
[17] Garfias-Mesias LF, Sykes JM, Tuck CDS. The effect of phase compositions on the pitting corrosion of 25 Cr duplex stainless steel in chloride solutions. Corros Sci 1996;38:1319–30.
[18] Gao Bo, Xu Tao, Wang Li, Liu Yi, Liu Junliang, Zhang Yaping, et al. Achieving a superior combination of tensile properties and corrosion resistance in AISI420 martensitic stainless steel by low-temperature tempering. Corros Sci 2023;225:111551.
[19] Nasery Isfahany A, Saghafian H, Borhani G. The effect of heat treatment on mechanical properties and corrosion behavior of AISI420 martensitic stainless steel. J Alloys Compd 2011;509:3931–6.
[20] Taji I, Moayed MH, Mirjalili M. Correlation between sensitisation and pitting corrosion of AISI 403 martensitic stainless steel. Corros Sci 2015;92:301–8.
[21] Chandra K, Kain Vivekanand, Tewari R. Microstructural and electrochemical characterisation of heat-treated 347 stainless steel with different phases. Corros Sci 2013;67:118–29.
[22] Wang Li, Dong Chaofang, Yu Qiang, Man Cheng, Hu Yabo, Dai Zongbiao, et al. The correlation between the Distribution/Size of carbides and electrochemical behavior of 17Cr-1Ni ferritic-martensitic stainless steel. Metall Mater Trans A 2019;50:388–400.
[23] Man Cheng, Dong Chaofang, Cui Zhongyu, Xiao Kui, Yu Qiang, Li Xiaogang. A comparative study of primary and secondary passive films formed on AM355 stainless steel in 0.1M NaOH. Appl Surf Sci 2018;427:763–73.
[24] Feng Hao, Li Hua-Bing, Jiao Wei-Chao, Jiang Zhou-Hua, Cai Ming-Hui, Zhu Hong-Chun, et al. Significance of partial substitution of carbon by nitrogen on strengthening and toughening mechanisms of high nitrogen Fe-15Cr-1Mo-CN martensitic stainless steels. Metall Mater Trans A 2019;50:4987–99.

[25] Ha HeonYoung, Kwon HyukSang. Effects of Cr2N on the pitting corrosion of high nitrogen stainless steels. Electrochim Acta 2007;52:2175–80.
[26] Li Ni, Dong Chaofang, Man Cheng, Xiao Li, Kong Decheng, Ji Yucheng, et al. Insight into the localized strain effect on micro-galvanic corrosion behavior in AA7075-T6 aluminum alloy. Corros Sci 2021;180:109174.
[27] Li Wenyao, Guo Tao, Xu Lining, Chen Lin, Jiang Baolong, Wang Xuehan, et al. Promotion of pitting corrosion at hydrogen-enriched α/γ phase boundaries in austenitic stainless steel weld joints. Acta Mater 2022;227:117728.
[28] Hai Chao, Zhu Yuetong, Fan Endian, Du Cuiwei, Cheng Xuequn, Li Xiaogang. Effects of the microstructure and retained/reversed austenite on the corrosion behavior of NiCrMoV/Nb high-strength steel. npj Mater Degrad 2023;7:40.
[29] Ji Yucheng, Fu Xiaoqian, Safyari Mahdieh, Yao Chenyang, Shuang Fei, Cheng Xuequn, et al. Tailoring precipitates for enhanced hydrogen trapping in aluminum alloys. Nat Commun 2026;17:279.
[30] Yao Jizheng, Li Ni, Grothe Hinrich, Qi Zhenhui, Dong Chaofang. Determination of the hydrogen effects on the passive film and the micro-structure at the surface of 2205 duplex stainless steel. Appl Surf Sci 2021;554:149597.
[31] Ji Yucheng, Fu Xiaoqian, Dey Poulumi, Dong Chaofang. Revealing hydrogen dynamics and embrittlement resistance in Cu-modified Al-Sc alloys using machine learning potential. Mater Lett 2026;409:140170.
[32] Ji Yucheng, Fu Xiaoqian, Ding Feng, Xu Yongtao, He Yang, Ao Min, et al. Artificial intelligence combined with high-throughput calculations to improve the corrosion resistance of AlMgZn alloy. Corros Sci 2024;233:112062.
[33] Xue Wei, Wang Yixuan, Xia Jiuyang, Zhang Zequn, Huang Kang, Lu Shuai, et al. Initial localized corrosion induced by multiscale precipitates in the new generation high-strength Al-Zn-Mg-Cu alloy. Corros Sci 2023;224:111516.
[34] Lu Si-Yuan, Yao Ke-Fu, Chen Yun-Bo, Wang Miao-Hui, Shao Yang, Ge Xue-Yuan. Effects of austenitizing temperature on the microstructure and electrochemical behavior of a martensitic stainless steel. J Appl Electrochem 2015;45:375–83.
[35] Xu Hai-feng, Wu Gui-lin, Wang Chang, Li Jian, Cao Wen-quan. Microstructure, hardness and contact fatigue properties of X30N high nitrogen stainless bearing steel. J Iron Steel Res Int 2018;25:954–67.
[36] Sathirachinda Namurata, Pettersson Rachel, Wessman Sten, Pan Jinshan. Study of nobility of chromium nitrides in isothermally aged duplex stainless steels by using SKPFM and SEM/EDS. Corros Sci 2010;52:179–86.
[37] Luo H, Dong CF, Li XG, Xiao K. The electrochemical behaviour of 2205 duplex stainless steel in alkaline solutions with different pH in the presence of chloride. Electrochim Acta 2012;64:211–20.
[38] Yao Jizheng, Macdonald Digby D, Dong Chaofang. Passive film on 2205 duplex stainless steel studied by photo-electrochemistry and ARXPS methods. Corros Sci 2019;146:221–32.
[39] Yue Xiaoqi, Chen Dihao, Krishnan Anantha, Tidesten Magnus, Larsson Alfred, Tong Haijie, et al. In depth analysis of the passive film on martensitic tool alloy: effect of tempering temperature. Corros Sci 2024;234:112133.
[40] Yuan Feng, Wei Gaoyang, Gao Shurui, Lu Siyuan, Liu Hengsan, Li Shuxin, et al. Tuning the pitting performance of a Cr-13 type martensitic stainless steel by tempering time. Corros Sci 2022;203:110346.
[41] Lee Jae-Bong, Kim Suk-Won. Semiconducting properties of passive films formed on Fe–Cr alloys using capacitiance measurements and cyclic voltammetry techniques. Mater Chem Phys 2007;104:98–104.
[42] Piao Tiehua, Park Su-Moon. Spectroelectrochemical studies of passivation and transpassive breakdown reactions of stainless steel. J Electrochem Soc 1997;144:3371.
[43] Zhang Yancheng, Urquidi-Macdonald Mirna, Engelhardt George R, Macdonald Digby D. Development of localized corrosion damage on low pressure turbine disks and blades: I. Passivity. Electrochim Acta 2012;69:1–11.
[44] Kumar Bonagani Sunil, Bathula Vishwanadh, Kain Vivekanand. Influence of tempering treatment on microstructure and pitting corrosion of 13 wt.% Cr martensitic stainless steel. Corros Sci 2018;131:340–54.
[45] Guitián B, Nóvoa XR, Puga B. Electrochemical impedance spectroscopy as a tool for materials selection: water for haemodialysis. Electrochim Acta 2011;56:7772–9.
[46] Guiñón-Pina V, Igual-Muñoz A, García-Antón J. Influence of pH on the electrochemical behaviour of a duplex stainless steel in highly concentrated LiBr solutions. Corros Sci 2011;53:575–81.
[47] Kocijan Aleksandra, Merl Darja Kek, Jenko Monika. The corrosion behaviour of austenitic and duplex stainless steels in artificial saliva with the addition of fluoride. Corros Sci 2011;53:776–83.
[48] Sun Li, Zhao Tianyu, Qiu Jie, Sun Yangting, Li Weihua, Zheng Haibing, et al. Mixed potential model for passivity characters of hyper-duplex stainless steel 2707 in ammonium carbonate solution containing chloride. Corros Sci 2022;201:110302.
[49] Cui Zhongyu, Wang Liwei, Ni Hongtao, Hao Wenkui, Cheng Man, Chen Shuangshuai, et al. Influence of temperature on the electrochemical and passivation behavior of 2507 super duplex stainless steel in simulated desulfurized flue gas condensates. Corros Sci 2017;118:31–48.
[50] Zhao Tianyu, Chen Si, Qiu Jie, Sun Li, Macdonald Digby D. Study on the passivation properties of austenitic stainless steel 316LN based on the point defect model. Corros Sci 2024;237:112293.
[51] Serdar Marijana, Valek Žulj Lidija, Bjegović Dubravka. Long-term corrosion behaviour of stainless reinforcing steel in mortar exposed to chloride environment. Corros Sci 2013;69:149–57.
[52] Jorcin Jean-Baptiste, Orazem Mark E, Pébère Nadine, Tribollet Bernard. CPE analysis by local electrochemical impedance spectroscopy. Electrochim Acta 2006;51:1473–9.
[53] Wang Li, Dong Chaofang, Yao Jizheng, Dai Zongbiao, Man Cheng, Yin Yupeng, et al. The effect of η-Ni3Ti precipitates and reversed austenite on the passive film stability of nickel-rich custom 465 steel. Corros Sci 2019;154:178–90.
[54] Zhou ZhiYou, Tian Na, Li JunTao, Broadwell Ian, Sun ShiGang. Nanomaterials of high surface energy with exceptional properties in catalysis and energy storage. Chem Soc Rev 2011;40:4167–85.
[55] Li W, Li DY. Variations of work function and corrosion behaviors of deformed copper surfaces. Appl Surf Sci 2005;240:388–95.
[56] Erazmus-Vignal P, Vignal V, Saedlou S, Krajcarz F. Corrosion behaviour of sites containing (Cr, Fe)2N particles in thermally aged duplex stainless steel studied using capillary techniques, atomic force microscopy and potentiostatic pulse testing method. Corros Sci 2015;99:194–204.
[57] Ahn SeJin, Kwon HyukSang, Macdonald Digby D. Role of chloride ion in passivity breakdown on iron and nickel. J Electrochem Soc 2005;152:B482.
[58] Ilevbare GO, Burstein GT. The role of alloyed molybdenum in the inhibition of pitting corrosion in stainless steels. Corros Sci 2001;43:485–513.
[59] Sunil Kumar B, Kain Vivekanand, Vishwanadh B. Effect of tempering treatments on microstructure and intergranular corrosion of 13 wt% Cr martensitic stainless steel. Corrosion 2016;73:362–78.
[60] Qiao Yanxin, Wang Xinyi, Yang Lanlan, Wang Xiaojing, Chen Jian, Wang Zhengbin, et al. Effect of aging treatment on microstructure and corrosion behavior of a Fe-18Cr-15Mn-0.66N stainless steel. J Mater Sci Technol 2022;107:197–206.
[61] Mao Feixiong, Dong Chaofang, Sharifi-Asl Samin, Lu Pin, Macdonald Digby D. Passivity breakdown on copper: influence of chloride ion. Electrochim Acta 2014;144:391–9.
[62] Hakiki NE, Montemor MF, Ferreira MGS, Belo M da Cunha. Semiconducting properties of thermally grown oxide films on AISI 304 stainless steel. Corros Sci 2000;42:687–702.
[63] Luo Hong, Su Huaizhi, Dong Chaofang, Li Xiaogang. Passivation and electrochemical behavior of 316L stainless steel in chlorinated simulated concrete pore solution. Appl Surf Sci 2017;400:38–48.
[64] Nicic Igor, Macdonald Digby D. The passivity of Type 316L stainless steel in borate buffer solution. J Nucl Mater 2008;379:54–8.
[65] Macdonald Digby D. The history of the point defect model for the passive state: a brief review of film growth aspects. Electrochim Acta 2011;56:1761–72.
[66] Zhang H, Xue P, Wu LH, Song QN, Wang D, Xiao BL, et al. Effect of grain ultra-refinement on corrosion behavior of ultra-high strength high nitrogen stainless steel. Corros Sci 2020;174:108847.
[67] Fu Yao, Wu Xinqiang, Han En-Hou, Ke Wei, Yang Ke, Jiang Zhouhua. Effects of nitrogen on the passivation of nickel-free high nitrogen and manganese stainless steels in acidic chloride solutions. Electrochim Acta 2009;54:4005–14.
[68] Luo Hong, Yu Qiang, Dong Chaofang, Sha Gang, Liu Zhenbao, Liang Jianxiong, et al. Influence of the aging time on the microstructure and electrochemical behaviour of a 15-5PH ultra-high strength stainless steel. Corros Sci 2018;139:185–96.
[69] Clayton Clive R, Halada Gary P, Kearns Jeffery R. Passivity of high-nitrogen stainless alloys: the role of metal oxyanions and salt films. Mater Sci Eng, A 1995;198:135–44.
[70] Jun Li, Wang Qingchuan, Yang Yixun, Wu Zhiqiang, Tan Lili, Ren Yibin, et al. Enhancing pitting corrosion resistance of severely cold-worked high nitrogen austenitic stainless steel by nitric acid passivation. J Electrochem Soc 2019;166:C365.
[71] Chen Longjun, Liu Wei, Dong Baojun, Zhao Yonggang, Zhang Tianyi, Fan Yueming, et al. Insight into electrochemical passivation behavior and surface chemistry of 2205 duplex stainless steel: effect of tensile elastic stress. Corros Sci 2021;193:109903.
[72] Sun Shicheng, Wei Sufeng, Wang Guoyong, Jiang Zhonghao, Lian Jianshe, Ji Changtao. The synthesis and electrochemical behavior of high-nitrogen nickel-free austenitic stainless steel. J Mater Eng Perform 2014;23:3957–62.
[73] Lu YC, Ives MB, Clayton CR. Synergism of alloying elements and pitting corrosion resistance of stainless steels. Corros Sci 1993;35:89–96.
[74] Baba H, Kodama T, Katada Y. Role of nitrogen on the corrosion behavior of austenitic stainless steels. Corros Sci 2002;44:2393–407.
[75] Vignal V, Krawiec H, Heintz O, Mainy D. Passive properties of lean duplex stainless steels after long-term ageing in air studied using EBSD, AES, XPS and local electrochemical impedance spectroscopy. Corros Sci 2013;67:109–17.